

1 **Measurement report: Hygroscopicity of Size-Selective Aerosol  
2 Particles at Heavily Polluted Urban Atmosphere of Delhi:  
3 Impacts of Chloride Aerosol**

4 Anil Kumar Mandariya<sup>1,2</sup>, Ajit Ahlawat<sup>3</sup>, Mohd. M. V. Haneef<sup>1</sup>, Nisar A. Baig<sup>1</sup>, Kanan  
5 Patel<sup>4</sup>, Joshua S. Apte<sup>5</sup>, Lea Hildebrandt Ruiz<sup>4</sup>, Alfred Wiedensohler<sup>3\*</sup>, and Gazala Habib<sup>1\*</sup>

6 <sup>1</sup>Department of Civil Engineering, Indian Institute of Technology Delhi, New Delhi, India

7 <sup>2</sup>now at: Univ Paris Est Creteil and University Paris Cité, CNRS, LISA, F – 94010 Créteil, France

8 <sup>3</sup>Leibniz Institute for Tropospheric Research (TROPOS), Permoserstraße, 15 Leipzig, Germany

9 <sup>4</sup>Department of Civil, Architectural and Environmental Engineering, The University of Texas at Austin, Austin,  
10 Texas, USA

11 <sup>5</sup>McKetta Department of Chemical Engineering, The University of Texas at Austin, Austin, Texas, USA

12 *Correspondence to:* Gazala Habib (gazalahabib@civil.iitd.ac.in) and Alfred Wiedensohler (ali@tropos.de)

13 **Abstract.** Recent research has unveiled the pivotal role of wintertime episodic high chloride emissions in the  
14 Delhi region, which significantly influence aerosol hygroscopicity and aerosol-bound liquid water, thereby  
15 contributing to the initiation of fog episodes in Delhi. However, these findings have primarily relied on modeled  
16 aerosol hygroscopicity, necessitating validation through direct hygroscopicity measurements. In this study, we  
17 present the measurement results of bulk aerosol composition of non-refractory PM<sub>1</sub> from ACSM and size-resolved  
18 (Nucleation, Aitken, and Accumulated mode particles) hygroscopic growth factor and associated hygroscopicity  
19 parameter at 90% relative humidity (RH) measured using H-TDMA (Hygroscopic-Tandem Differential Mobility  
20 Analyser) at Delhi Aerosol Supersite (DAS) for the first time. Our observations indicate that the hygroscopicity  
21 parameter ( $\kappa_{H-TDMA, 90\%}$ ) ranges from 0.00 to 0.11 (with an average of  $0.03 \pm 0.02$ ) for 20 nm aerosol particles,  
22 0.05 to 0.22 ( $0.11 \pm 0.03$ ) for 50 nm particles, 0.05 to 0.30 ( $0.14 \pm 0.04$ ) for 100 nm particles, 0.05 to 0.41 ( $0.18 \pm 0.06$ ) for 150 nm particles, and 0.05 to 0.56 ( $0.22 \pm 0.07$ ) for 200 nm particles. Remarkably, our results reveal  
23 that the period characterized by high chloride (H-Cl) emissions exhibits significantly higher hygroscopicity ( $0.35 \pm 0.06$ )  
24 compared to periods marked by high biomass burning (H-BB) ( $0.18 \pm 0.04$ ), high hydrocarbon-like  
25 organic aerosol (H-HOA) ( $0.17 \pm 0.05$ ), and relatively cleaner periods ( $0.27 \pm 0.07$ ). This study provides first  
26 observational evidence of Ammonium Chloride as the major contributor to aerosol hygroscopic growth and liquid  
27 water content in Delhi, which highlights the role of Ammonium Chloride in aerosol-water interaction and related  
28 haze/fog development. Additionally, the high chloride content in aerosols appears to counteract the negative  
29 effects of high organic aerosol (OA) levels on cloud condensation nuclei (CCN) activity.

Mis en forme : Indice

Déplacé (insertion) [1]

**Supprimé:** The high chloride (H-Cl) period was observed significantly ( $p<0.05$ ) higher hygroscopicity ( $0.35 \pm 0.06$ ) compared to high biomass burning (H-BB) ( $0.18 \pm 0.04$ ), high hydrocarbon-like organic aerosol (H-HOA) ( $0.17 \pm 0.05$ ), and relatively cleaner period ( $0.27 \pm 0.07$ ).

38 **1. Introduction**

39 The Intergovernmental Panel on Climate Change (IPCC) reported that aerosol-cloud interaction is still not fully  
40 understood and has significant uncertainties in quantifying global radiative budgets. Aerosol hygroscopicity plays  
41 a pivotal role in overcoming and explaining these uncertainties. Hygroscopicity is crucial to understand how the  
42 aerosol particles act as cloud condensation nuclei (CCN) and forms fog droplets/haze at sub-saturated/nearly  
43 saturation and cloud droplets at atmospheric supersaturation levels (McFiggans et al., 2006; Topping and  
44 McFiggans, 2012). Its understanding is crucial to predict the aerosol size distribution and scattering properties  
45 better in global models under varying atmospheric humidity (RH) conditions (Randall et al., 2007).  
46 Hygroscopicity at higher RH atmospheric conditions leads to an enhanced aerosol cross-sectional area, resulting  
47 in efficient light scattering by the aerosol particles (Tang and Munkelwitz, 1994). It mainly depends on particle  
48 size and chemical composition. Generally, the inorganic salts such as ammonium salts of sulfate, nitrate, and  
49 chloride, are highly hygroscopic (Hu et al., 2011; Petters and Kreidenweis, 2007), organic aerosol (OA) are  
50 comparatively less hygroscopic (Jimenez et al., 2009; Kroll et al., 2011), while dust particles and black/elemental  
51 carbon particles are stated as hydrophobic (Seinfeld and Pandis, 2006). Further, the elevated atmospheric RH  
52 during winter and monsoon favour the formation of more oxidized secondary organic aerosol (SOA) via aqueous-  
53 phase (Ervens et al., 2011) and heterogeneous reactions (McNeill, 2015), leads to enhancement in organic aerosol  
54 hygroscopicity (Jimenez et al., 2009; Mei et al., 2013) which adversely impact on the local visibility (Li et al.,  
55 2016; Liu et al., 2012). However, aerosol loading inversely affects aerosol hygroscopicity (Mandariya et al.,  
56 2020a). Apart from it, aerosol loading is also a critical factor in deciding the lifetime of cloud, which affects the  
57 region's rain quantitatively (Albrecht, 1989; Lohmann and Feichter, 2005).  
58 Over the past decades, aerosol hygroscopicity has been intensively measured using hygroscopic tandem  
59 differential mobility analyzer (H-TDMA) (Massling et al., 2005; Gysel et al., 2007; Mandariya et al., 2020;  
60 Swietlicki et al., 2008; Yeung et al., 2014; Kecorius et al., 2019) and CCN (Bhattu and Tripathi, 2015; Gunthe et  
61 al., 2011; Massoli et al., 2010; Ogawa et al., 2016) counter under sub- and supersaturation levels, respectively.  
62 Petters and Kreidenweis (2007) introduced a hygroscopicity parameter, kappa ( $\kappa$ ), to associate aerosol  
63 hygroscopicity with its chemical composition. Furthermore, hygroscopicity associated with OA potentially varies  
64 with OA chemical properties like solubility, the extent of dissociation in aerosol water, and surface activity  
65 (Hallquist et al., 2009; Jimenez et al., 2009), leads to difficulty in the quantification of OA hygroscopicity, result  
66 in introducing more discrepancies in predicted and measured aerosol hygroscopicity. Hence, there is a need to

**Supprimé:** Recent studies reveal that wintertime chloride emission in the Delhi region is crucial in governing enhancement to theoretically calculated aerosol hygroscopicity and aerosol-bound liquid water to trigger Delhi's fog episodes. Here, we reported that the high volume fractional contribution of ammonium chloride into aerosol governs the high aerosol hygroscopicity and associated liquid water content based on the experimental data first time in Delhi. The episodically high chlorides bonded with excess ammonia present in Delhi's atmosphere, which could lead to haze and fog formation under high relative humidity in the region. Therefore, our study suggests that controlling the plastic-contained waste, open burning, and e-waste industrial chloride emission could significantly minimize Delhi's heavily polluted haze/fog events. The high chloride (H-Cl) period was observed significantly ( $p < 0.05$ ) higher hygroscopicity ( $0.35 \pm 0.06$ ) compared to high biomass burning (H-BB) ( $0.18 \pm 0.04$ ), high hydrocarbon-like organic aerosol (H-HOA) ( $0.17 \pm 0.05$ ), and relatively cleaner period ( $0.27 \pm 0.07$ ). ¶

In this study, we present the measurement results of bulk aerosol composition of non-refractory PM<sub>1</sub> from ACSM and size-resolved (Nucleation, Aitken, and Accumulated mode particles) hygroscopic growth factor and associated hygroscopicity parameter at 90% relative humidity (RH) measured using H-TDMA at Delhi Aerosol Supersite (DAS) first time. The hygroscopic parameter ( $\kappa_{H-TDMA, 90\%}$ ) was significantly ( $p < 0.05$ ) enhanced with the size of the particles. The observed  $\kappa_{H-TDMA, 90\%}$  ranged from  $0.00$  to  $0.11$  ( $0.03 \pm 0.02$ ),  $0.05$  to  $0.22$  ( $0.11 \pm 0.03$ ),  $0.05$  to  $0.30$  ( $0.14 \pm 0.04$ ),  $0.05$  to  $0.41$  ( $0.18 \pm 0.06$ ), and  $0.05$  to  $0.56$  ( $0.22 \pm 0.07$ ) for 20, 50, 100, 150, and 200 nm aerosol particles, respectively. The Inorganic-to-organic aerosol ratio in aerosol modulated mainly the aerosol hygroscopicity. In addition, the accumulation mode particle's hygroscopicity was regulated potentially by the volume fraction of NH<sub>4</sub>Cl and OA in aerosol particles. Interestingly, our results reveal that the daytime flattening pattern of accumulation aerosol particles in diurnal variation is potentially due to counter the effect of increment of (NH<sub>4</sub>)<sub>2</sub>SO<sub>4</sub> and NH<sub>4</sub>NO<sub>3</sub> and decrement of NH<sub>4</sub>Cl and OA in aerosol particles. ¶

**Mis en forme :** Espace Avant : 12 pt, Après : 12 pt

**Déplacé vers le haut [1]:** The high chloride (H-Cl) period was observed significantly ( $p < 0.05$ ) higher hygroscopicity ( $0.35 \pm 0.06$ ) compared to high biomass burning (H-BB) ( $0.18 \pm 0.04$ ), high hydrocarbon-like organic aerosol (H-HOA) ( $0.17 \pm 0.05$ ), and relatively cleaner period ( $0.27 \pm 0.07$ ). ¶

**Mis en forme :** Indice

114 explore measurement-based aerosol hygroscopicity for Delhi's atmosphere to understand the frequent haze/cloud  
115 formations better.

116 In past decades, fast economic growth and industrialization in the [Indo Gangetic Plain \(IGP\)](#) led to severe air  
117 quality during wintertime (Wester et al., 2019). Delhi is potentially affected by local and regional air pollution  
118 problems in wintertime (Arub et al., 2020; Bhandari et al., 2020; Gani et al., 2019; Prakash et al., 2018). Recent  
119 studies (Gani et al., 2019; Rai et al., 2020) have shown chloride is one of the predominant factors to degrade the  
120 air quality in the Delhi region and significantly favour the haze/fog formation during winter (Gunthe et al., 2021).  
121 Trash and biomass burning for heating and waste degradation are among the main contributors to chloride in Delhi  
122 (Rai et al., 2020). A recent study conducted in Delhi reported that frequent high chloride events promotes high  
123 aerosol liquid water content under elevated humid condition leads to haze and poor visibility in the city (Chen et  
124 al., 2022). In addition, Gunthe et al. (2021) showed higher chloride also facilitates enhancement in aerosol  
125 hygroscopicity, however, this study was based on theoretical hygroscopicity. Therefore, it is essential to investigate  
126 the impacts of chloride on aerosol hygroscopicity and its potential to enhance aerosol-bound liquid water based  
127 on field measurements. Moreover, the hygroscopicity of the aerosol particles in the heavily polluted urban  
128 atmosphere, which confines to highly complex composition, is [extremely](#) limited, like Delhi, situated at Indo  
129 Gangetic Plain (IGP), India, where air quality severely degrades during haze/fog-dominated. To the author's best  
130 knowledge, the current study is first in Delhi, India, exploring a complex atmosphere of IGP using H-TDMA-  
131 measured aerosol hygroscopicity. Hence, it is essential to measure size-resolved aerosol hygroscopicity in Delhi's  
132 atmosphere and investigate its role in the context of high chloride.

**Supprimé:** very

## 133 **2. Experimental Methods**

### 134 **2.1 Aerosol Measurements**

135 Real-time atmospheric aerosol measurements were conducted simultaneously using Hygroscopic-Tandem  
136 Differential Mobility Analyzer (H-TDMA), [Mobility Particle Size Spectrometer \(MPSS\)](#), and Aerodyne Aerosol  
137 Chemical Speciation Monitor (ACSM, Aerodyne Research, Billerica MA) during winter (1<sup>st</sup> February 2020 to  
138 16<sup>th</sup> March 2020) at the Indian Institute of Technology (IIT) Delhi in Block 5, at the height of nearly 15 m [above](#)  
139 [ground level \(a.g.l.\) as shown in Fig. 1. The lab-2 is situated at the height of 15 m a.g.l. and lab-2 is 50 m apart](#)  
140 [from lab-1.](#)

**Supprimé:** Details on the sampling site can be found in Arub et al. (2020).

141 In this study, the HTDMA system was used to investigate the hygroscopic growth of size-resolved particles at 90  
142 % RH. The HTDMA system has been previously used in many field campaigns (Massling et al., 2007; Wu et al.,

146 2013b; Zhang et al., 2016). The HTDMA system (TROPOS, Germany) is comprised of two Differential Mobility  
147 Analyzers (DMAs, type Hauke-median, TROPOS, Germany), a Condensation Particle Counter (CPC, Model  
148 3772, TSI Inc., USA) along with a humidifier system located between the two DMAs. The role of first DMA is  
149 to select the quasi-monodisperse particles at a dry diameter ( $D_p$ , dry) with 30% RH. After that, the size-selected  
150 particles pass through a humidity conditioner, which can be adjusted from 30% to 90% RH by regulating the  
151 aerosol and sheath air flow by mixing dry air with RH<5% and humid air with ~95% RH (Maßling et al., 2003).  
152 The uncertainties associated with RH measurement at 90% RH is 1.0%. The particle hygroscopic growth  
153 distribution at dry size ( $D_p$ , dry) at a certain humidity can be easily determined with CPC. There are two humidity  
154 sensors (Vaisala) in the system for aerosol and sheath respectively. The humidity sensors positioned in the second  
155 DMA were calibrated automatically with 100 nm ammonium sulfate ( $(\text{NH}_4)_2\text{SO}_4$ ) particles every 30 min at 90%  
156 RH to analyze the stability at high RH. The measurement error of the HTDMA mainly depends on the uncertainty  
157 in measuring and controlling the RH within the system (Su et al., 2010). Therefore, all RH sensors were calibrated  
158 using the Vaisala salt kit comprising LiCl, NaCl, KCl etc. prior the measurement campaign. Both the DMAs were  
159 size calibrated by applying the Latex particles with the standard size of 200 nm before the start of the measurement.  
160 The number concentration peak occurred at 203 nm, referring to accuracy of DMAs size selection at 1.5%.  
161 HTDMA system was operated at 90% RH to measure the hygroscopic growth factors (HGFs) for particles with  
162  $D_p$ , dry of five different sizes i.e. 20, 50, 100, 150 and 200 nm. The time resolution of the full scan covering the  
163 five sizes was about 30 min.

164 Particle number size distributions (PNSDs) and particle volume-size distributions (PVSDs) were measured using  
165 a Mobility Particle Size Spectrometer (MPSS (TROPOS type)).

166 A Detailed description of ACSM setup can be found in Arub et al. (2020). ACSM was operated at nearly 0.1 lpm  
167 at 1 min time resolution in a temperature-controlled laboratory. ACSM was set to run to measure mass-to-charge  
168 ratio (m/z) m/z 10 to m/z 140. The ACSM measures non-refractory particulate matter less than 1 $\mu\text{m}$  (NR-PM<sub>1</sub>).  
169 The concentrate PM<sub>1</sub> aerosol beam was impacted on the vaporizer at 600 °C and flash-vaporized compounds were  
170 subsequently ionized through impact ionization at 70 eV electron and detected with a quadrupole mass  
171 spectrometer (Ng et al., 2011). The 200 ms amu<sup>-1</sup> scan speed and pause setting at 125 for a sampling time (64 s)  
172 were set to acquire aerosol mass spectra in ACSM. Detailed operational procedures for the ACSM are explained  
173 elsewhere in Gani et al. (2019).

**Mis en forme :** Police :Non Italique

**Mis en forme :** Indice

**Mis en forme :** Police :Non Italique

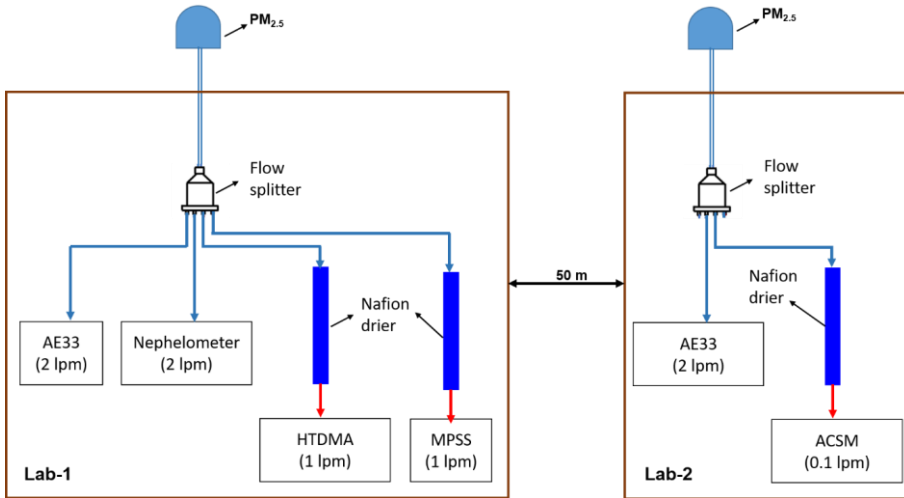
**Mis en forme :** Indice

**Mis en forme :** Police :Non Italique

**Mis en forme :** Indice

**Supprimé:**

**Supprimé:** ¶



177 **Figure 1: Schematic diagram of the inlet systems for aerosol sampling instruments. The blue and red**  
 178 **sampling lines indicate the ambient air and dehumidified (RH<25%) ambient air, respectively.**

## 179 2.2 Meteorological and Gas Data

180 The gas data was taken from the location site R.K Puram -DPCC, a continuous ambient air quality monitoring  
 181 station controlled by the central control room for air quality management (Delhi-NCR). The gas data were  
 182 downloaded from the CPCB website (<https://app.cpcbccr.com/CCR/#/caaqm-dashboard/caaqm-landing/data>). R.K.  
 183 Puram is located 3.5 km northwest of IIT Delhi. The wind speed (WS), wind direction (WD), temperature (T),  
 184 and relative humidity (RH) were continuously measured using an automatic weather station (Watch Dog 2000  
 185 series). The weather station is mounted over the top of the 9<sup>th</sup>-floor building of the IITD.

## 186 2.3 Data Analysis

### 187 2.3.1 H-TDMA

188 Overall, we recorded 1483 H-TDMA scans cycles. Afterward, the % difference between measured and theoretical  
 189 growth factors ( $\Delta q$ ) was calculated after each scan cycle for 100 nm ammonium sulfate particles. Those scan  
 190 cycles came between  $\Delta q \leq \pm 5\%$ , were only carried out for further data treatment, and the rest scans cycles were  
 191 discarded (Kecorius et al., 2019). Thus, we had 1102 H-TDMA scan cycles following this data quality check.  
 192 Regarding good scan cycles, we had 1449, 1431, 1438, 1470, and 1420 good H-TDMA scans for 20, 50, 100,  
 193 150, and 200 nm particles, respectively, to further analyze. Afterward that, a piecewise linear TDMAinv

**Mis en forme : Police :Gras**

**Supprimé: 2**

**Supprimé: 2.2.1 ACSM**

Details on ACSM calibration and data processing are in Patel et al., 2021. We conducted Positive matrix factorization (PMF) on the data and found a four-factor solution (hydrocarbon-like OA, "HOA"; biomass burning OA, "BBOA"; less-oxidized OA, "LO-OOA"; more-oxidized OA "MO-OOA") to best represent the data set. Further details about PMF analysis are in section S.1 of the SI. The windrose plot was plotted by openair in R package (<http://www.r-project.org>, <http://www.openair-project.org>). The 48-hour back trajectory of air masses reaching Delhi super site (DSL) at 500 m above the ground at every hour for the entire study period was estimated by an offline based Hybrid Single-Particle Lagrangian Integrated Trajectory (HYSLIT4) model developed by NOAA/Air Resources Laboratory (ARL) (Draxler and Hess, 1997). The input meteorological data for back trajectories were taken from the Global Data Assimilation System (GDAS 0.5 degree) archive maintained by ARL (<http://ready.arl.noaa.gov/archives.php>). Further, utilizing these estimated back trajectories as input combined with the measured mass fraction of chemical species of bulk aerosol, Potential Source Contribution Function (PSCF) analysis was carried out with the help of a tool called Zefir (V 3.7) written in Igor Pro (WaveMetrics). Detail description regarding Zefir tool can be found elsewhere (Petit et al., 2017). In addition, box plots reported in the subsequent section were also plotted with the help of this tool. The aerosol liquid water content (ALWC) as a function of inorganic species mass concentration, ambient temperature (T), and ambient relative humidity (RH), was calculated by ISORROPIA-II model (Fountoukis and Nenes, 2007).¶

**Supprimé: 2**

**Supprimé: 2**

**Supprimé:** The humidity sensor of DMA2 was automatically calibrated with 100 nm ammonium sulfate particles after each scan cycle.

**Supprimé:** say

233 algorithm, namely TDMAinv Toolkit, written in IgorPro and developed by Gysel et al. (2009), was used to do  
234 post-data treatment on the raw HGF. Because the measured distribution function is a skewed and smoothed  
235 integral transform of the actual growth factor probability density functions (GF-PDFs). A detailed description of  
236 the raw data processing in the TDMAinv toolkit to measure real HGFs is described in Gysel et al. (2009). The  
237 TDMAinv toolkit was successfully used in various studies around the globe (Gysel et al., 2007; Liu et al., 2012;  
238 Sjogren et al., 2007; Wang et al., 2018a) and at Kanpur, India (Mandariya et al., 2020a). Besides, the RH in the  
239 DMA2 generally achieved the set value of 90% and remained stable within  $\pm 1\%$ , although occasionally, it faced  
240 a more considerable drift. All growth factors measured between 88 and 92% RH were corrected to a target value  
241 of 90% (HGF\_90%) (Gysel et al., 2007) using the kappa-model suggested in the TDMAinv toolkit (Gysel et al.,  
242 2009) to minimize this DMA2 RH drifts. After it, 979, 957, 972, 969, and 966 scans were found corrected at target  
243 RH for 20, 50, 100, 150, and 200 nm aerosol particles, respectively, which further averaged for 60 min time  
244 resolution and finally, these numbers reached to 425, 429, 419, 424, and 417, respectively.

245 Further, size-resolved hygroscopicity factors (kappa,  $\kappa$ , say  $\kappa_{H-TDMA\_90\%}$ ) were calculated from the respective size-  
246 resolved target RH corrected HGFs using equation (1) kappa-Köhler theory (Mandariya et al., 2020a; Petters and  
247 Kreidenweis, 2007).

$$248 \quad \kappa_{H-TDMA\_90\%} = (HGF\_90\%^3 - 1) \left[ \frac{1}{RH} \exp \left( \frac{4\sigma M_w}{RT \rho_w D_o HGF_{90\%}} \right) - 1 \right], \quad (1)$$

249 Where,  $\kappa_{H-TDMA\_90\%}$  is the hygroscopicity factor at 90% RH, HGF\_90% is the size-resolve HGF at 90% RH, RH  
250 is the atmospheric relative humidity in fraction,  $\sigma$  is the surface tension of the aerosol liquid droplet-air interface  
251 at the droplet surface in N/m and can be assumed nearly to pure water, R is the universal gas constant in J K<sup>-1</sup> mol<sup>-1</sup>,  
252  $M_w$  is the molecular mass of water, T is the ambient temperature in Kelvin (K),  $\rho_w$  is the density of water in  
253 kg/m<sup>3</sup>, and  $D_o$  is the dry mobility diameter of the particle in m.

254 **2.3.2 MPSS**

255 MPSS measures electrical mobility distribution, which is then converted to PNSD in the 8 to ~800 nm mobility  
256 diameter range by applying an inversion algorithm to correct for multiple charged aerosol particles (Wiedensohler,  
257 1988; Pfeiffer et al., 2014) and diffusional losses (Wiedensohler et al., 2012; 2018).

258

259

260 **2.3.3 ACSM**

261 An Aerodyne Aerosol Chemical Speciation Monitor (ACSM, Aerodyne Research, Billerica MA) provided mass  
262 concentrations of organic aerosol (OA), ammonium (NH<sub>4</sub>), sulfate (SO<sub>4</sub>), nitrate (NO<sub>3</sub>), and chloride (Cl). Details  
263 on ACSM calibration and data processing are in Patel et al., 2021. We conducted Positive matrix factorization  
264 (PMF) on the data and found a four-factor solution (hydrocarbon-like OA, "HOA"; biomass burning OA,  
265 "BBOA"; less-oxidized OA, "LO-OOA"; more-oxidized OA "MO-OOA) to best represent the data set. Further  
266 details about PMF analysis are in section S.1 of the SI. Furthermore, based on the mass concentration peaks of  
267 BBOA, HOA, and Cl in the temporal variation (Fig. 1), respectively, three different events were characterized: 1)  
268 High-residential or biomass burning (H-BB), 2) High-hydrocarbon-like OA (H-HOA), and 3) High-chloride (H-  
269 Cl) period. In addition, the "Clean Period" was defined where PM<sub>1</sub> loading was less than 25 percentiles ( $\leq 38.7$   
270  $\mu\text{g m}^{-3}$ ) of the sampling period. The starting and end time of the event was defined by the starting the increment  
271 in the concentration and reaching the starting value while the concentration decreased.

**Mis en forme :** Police :Gras

272 **2.3.4 Derived Secondary Inorganic Salts**

**Supprimé:** 2

273 The ACSM mainly measures OA, NO<sub>3</sub>, SO<sub>4</sub>, NH<sub>4</sub>, and Cl. Therefore, we adopted a simplified ion-pairing scheme  
274 reported by Gysel et al. (2007). However, Gysel et al. (2007) did not include NH<sub>4</sub>Cl in their ion-pairing scheme;  
275 therefore, we elaborated this scheme and made some modifications in this scheme to include ammonium chloride  
276 (ACl) in the calculation. Hence, our modified ion-pairing scheme includes NH<sub>4</sub>Cl (ACl), NH<sub>4</sub>NO<sub>3</sub> (AN),  
277 (NH<sub>4</sub>)<sub>2</sub>SO<sub>4</sub> (AS), NH<sub>4</sub>HSO<sub>4</sub> (ABS), and H<sub>2</sub>SO<sub>4</sub> (SA) are shown below:

**Mis en forme :** Indice

**Mis en forme :** Indice

**Mis en forme :** Indice

**Supprimé:** ABS

**Mis en forme :** Indice

278 **Case-1**  $R_{SO_4}$  (NH<sub>4</sub> to SO<sub>4</sub>)  $\leq 1$

279 SA =  $98.0795 \times \max(0, (n_S - n_A))$

280 ABS =  $115.11 \times n_A$

281 AS = 0

282 AN = 0

283 ACl = 0

284 **Case-2**  $1 < R_{SO_4} < 2$

287 SA = 0

288 ABS =  $115.11 \times ((2 \times n_S) - n_A)$

289 AS =  $132.1405 \times (n_S - n_A)$

290 AN = 0

291 ACI = 0

292 **Case-3  $R_{SO_4} \geq 2$**

293 SA = 0

294 ABS = 0

295 AS =  $132.1405 \times n_S$

296  $AN = \left( \min \left( \left( n_A - \left( \frac{ABS}{115.11} \right) - \left( \frac{(2 \times AS)}{132.1405} \right) \right), n_N \right) \right) \times 80.0434$

297  $ACI = \left( \min \left( n_C, \left( n_A - \left( \frac{ABS}{115.11} \right) - \left( \frac{2 \times AS}{132.1405} \right) - \left( \frac{AN}{80.0434} \right) \right) \right) \right) \times 53.54$

298 Here, n denotes the number of moles, whereas A, N, S, and C denotes the NH<sub>4</sub>, NO<sub>3</sub>, SO<sub>4</sub>, and Cl species. We  
299 also predicted these inorganic salts concentrations from the ISORROPIA v2.1 model using NH<sub>4</sub>, SO<sub>4</sub>, NO<sub>3</sub>, and  
300 Cl. We found a strong correlation and nearly unit slope (0.9999) between the calculated and modelled inorganic  
301 salts as presented in Fig. S1, which strongly justifies the new ion-pairing scheme adopted in this study.

**Supprimé:** figure

### 302 **2.3.5 Windrose and Potential Source Contribution Function (PSCF)**

**Mis en forme :** Police :Gras

303 The windrose plot was plotted by openair in R package (<http://www.r-project.org>, <http://www.openair-project.org>). The 48-hour back trajectory of air masses reaching Delhi super site (DSL) at 500 m above the ground  
304 at every hour for the entire study period was estimated by an offline based Hybrid Single-Particle Lagrangian  
305 Integrated Trajectory (HYSPLIT4) model developed by NOAA/Air Resources Laboratory (ARL) (Draxler and  
306 Hess, 1997). The input meteorological data for back trajectories were taken from the Global Data Assimilation

309 System (GDAS 0.5 degree) archive maintained by ARL (<http://ready.arl.noaa.gov/archives.php>). Further,  
310 utilizing these estimated back trajectories as input combined with the measured mass fraction of chemical species  
311 of bulk aerosol, Potential Source Contribution Function (PSCF) analysis was carried out with the help of a tool  
312 called Zefir (V 3.7) written in Igor Pro (WaveMetrics). Detail description regarding Zefir tool can be found  
313 elsewhere (Petit et al., 2017). In addition, box plots reported in the subsequent section were also plotted with the  
314 help of this tool. The aerosol liquid water content (ALWC) as a function of inorganic species mass concentration,  
315 ambient temperature (T), and ambient relative humidity (RH), was calculated by ISORROPIA-II model  
316 (Fountoukis and Nenes, 2007).

317 **3. Result and Discussions**

318 **3.1 Overview of meteorology, trace gases, and aerosol characterization**

319 Fig. 2 illustrates the hourly-resolved temporal variability of meteorological parameters, including relative  
320 humidity (RH), temperature (T), wind direction (WD), and wind speed (WS), as well as the particle number size  
321 distribution (PNSD), particle volume size distribution (PVSD), principal components in non-refractory PM<sub>4</sub>, and  
322 organic aerosol (OA) with their fractional mass contributions. Additionally, Fig. S5 displays the temporal  
323 variability of atmospheric gases, such as nitrogen oxides (NO<sub>x</sub>), carbon monoxide (CO), and sulfur dioxide (SO<sub>2</sub>).  
324 Delhi's winter climate is primarily influenced by a depression generated by Western Disturbances, resulting in  
325 cold waves in the region. The ambient relative humidity (RH) and temperature (T) exhibit variability in the range  
326 of 24.2% to 96.6% and 9.0 °C to 28.5 °C, respectively, with average values of  $56.0\% \pm 18.2\%$  and  $18.7\text{ }^{\circ}\text{C} \pm 4.2\text{ }^{\circ}\text{C}$ .  
327 These fluctuations indicate that Delhi's atmosphere transitions from being wet and cold in February to dry and  
328 relatively warm in March. Notably, nighttime conditions tend to be cooler and more humid compared to daytime  
329 throughout the sampling period. Ambient RH exhibits a diurnal pattern, with a peak in the early morning (06:00-  
330 07:00 hours) and a valley around midday (13:00-15:00 hours). In contrast, ambient temperature follows an  
331 opposing trend, rising during midday, which can be correlated with higher solar radiation during those hours (see  
332 Fig. 3a & b). The higher ambient temperature and peak O<sub>3</sub> concentration during midday (Fig. 3(i)) suggest the  
333 presence of daytime photo-oxidation processes (Nelson et al., 2023). The wind speed (WS) and wind direction  
334 (WD) varied from 0.0 to 5.6 ( $1.0 \pm 1.0$ ) m/s and 4.0 to 345.7 ( $197.1 \pm 84.4$ ) degrees from the North, respectively,  
335 as shown in Fig. S6. Predominant wind directions were WNW-WSW and E-ESE. These patterns suggest that the  
336 atmosphere remains relatively stagnant during the study period, and the measured aerosols likely represent  
337 emissions and local aerosol chemistry in Delhi.

**Mis en forme :** Indice

**Mis en forme :** Indice

**Mis en forme :** Indice

338 Additionally, ambient trace gases NO<sub>x</sub> and CO exhibit significant variability throughout the sampling period,  
339 peaking during local burning activities. Ambient NO<sub>x</sub> levels reach a maximum of 421.2 ppb (58.4 ± 61.9) during  
340 intense biomass burning activities. CO concentrations also peak during similar periods as NO<sub>x</sub> and vary from 0.0  
341 to 7.66 ppm (0.58 ± 0.79), as shown in Fig. S5. The diurnal variation of these trace gases is presented in Fig. 3 (f,  
342 g, h, and i), with two peaks (06:00-08:00 and 17:00-20:00 hours) associated with morning local biomass/trash  
343 burning emissions and nighttime traffic rush hours. In contrast, SO<sub>2</sub> follows a different trend, with dynamic  
344 variations ranging from 0.46 to 9.55 ppb (4.41 ± 1.20) and showing peaks in the morning (09:00-12:00 hours) and  
345 at midnight (21:00-02:00 hours) associated with the local industrial stack emissions.

346 The PM<sub>1</sub> particle number concentration ranges from 408 to 29,845 /cm<sup>3</sup> (11319 ± 5552). High particle number  
347 concentrations are typically associated with local burning events. The particle concentration increases in the  
348 evening (at 18:00 hours) and reaches its maximum value at midnight, suggesting the resumption of residential  
349 burning activity and traffic emissions. These activities likely contribute to the lower geometric mean diameter  
350 (GMD) of the particle number size distribution (PNSD, approximately 47 nm), which increases to nearly 87 nm,  
351 as shown in Fig. 3(t), indicating nighttime aging of organic aerosol. The hourly averaged mean diurnal GMD of  
352 PVSD varies from approximately 274 to 324 nm (Fig. 3(y)), with a mean value of 309.1 ± 33.1 nm, which is close  
353 to this study's higher-end particle size of 200 nm hygroscopicity measurement. Therefore, ACSM bulk aerosol  
354 composition is the most suitable choice for discussing the hygroscopicity of these particles.

355 The hourly time-resolved NR-PM<sub>1</sub> (say hereafter PM<sub>1</sub>) concentration varied from 9.0 to 357.9 µg/m<sup>3</sup>, averaging  
356 81.2 ± 56.6 µg/m<sup>3</sup>. This observation lies well within the boundary of 12.7-392 µg/m<sup>3</sup> (NR-PM<sub>1</sub>), reported by Gani  
357 et al. (2019) for the same sampling site. Prakash et al. (2018) reported that PM<sub>1</sub> mass concentration is 83% of  
358 PM<sub>2.5</sub>, representing the dominance of combustion-based particles. Further, we observed that ACSM measured  
359 PM<sub>1</sub> was highly correlated ( $r^2 = 0.83$ ,  $p < 0.05$ ) with MPSS measured PM<sub>1</sub>, assuming an effective aerosol density  
360 1.6 g/cm<sup>3</sup> (Fig. S2). The OA ranged between 1 and 293 (46.5 ± 39.6) µg/m<sup>3</sup> with the predominant fraction of PM<sub>1</sub>,  
361 consistent with the range of 53.3 to 166 (112) µg/m<sup>3</sup> observed during winter (December-February) at the same  
362 site (Gani et al., 2019). However, lower average OA concentration could be explained by the measuring period of  
363 February-March, as aerosol loading starts decreasing in February after reaching its peak in December-January  
364 (Gupta and Mandariya, 2013). The campaign average fractional contribution OA to PM<sub>1</sub> was 56%, ranging from  
365 1 to 84%. This high OA contribution in PM<sub>1</sub> is consistent with other studies conducted in IGP (Chakraborty et al.,  
366 2016a; Gani et al., 2019; Mandariya et al., 2019) and worldwide (Jimenez et al., 2009; Zhang et al., 2007). Peaked  
367 OA mass concentrations were noted between 21:00-23:00 hr (figure 2(k)), consistent with previous studies

**Mis en forme :** Indice

**Mis en forme :** Indice

**Supprimé:** Meteorological parameters provided a quick summary of the local weather conditions at the sampling site. Figure 1 shows the hourly resolved temporal variability of meteorological parameters (RH, T, WD, and WS), particle number size distribution (PNSD), particle volume size distribution (PVSD), principal components in non-refractory PM<sub>1</sub> and OA and their fractional mass contribution. In addition, the temporal variability in the atmospheric gases (NO<sub>x</sub>, CO, and SO<sub>2</sub>) have shown in figure S5. Delhi's winter climate is mainly influenced by a depression created by the Western Disturbances caused by cold waves in the region. The ambient relative humidity (RH) and temperature (T) variability between 24.2–96.6% and 9.0–28.5°C with an average ( $\pm 1$  STD) of 56.0 ± 18.2% and 18.7 ± 4.2°C, respectively, showed the Delhi's atmosphere was varied from wet and cold to dry and relatively warm from February to March, respectively. The nighttime was somewhat cold and humid compared to the daytime throughout the sampling. The ambient RH showed a diurnal pattern with a peak during early morning 06:00-07:00 hr and the valley during noontime 13:00-15:00 hr, while ambient temperature showed an opposite trend with a rise during noontime could be correlated with noontime higher solar radiation. This comparatively higher ambient temperature and O<sub>3</sub> peak concentration during noontime indicate the daytime photooxidation process.¶

The wind speed (WS) and wind direction (WD) varied from 0.0 to 5.6 (1.0 ± 1.0) m/s and 4.0 to 345.7 (197.1 ± 84.4) degrees from the North, respectively, as shown in figure S6. Predominant wind directions were WNW-WSW and E-ESE. It indicates that the atmosphere remained stagnant during the study period, and measured aerosol potentially represents Delhi's emissions and local aerosol chemistry.¶ Furthermore, ambient trace gases NO<sub>x</sub> and CO showed substantial variability during the sampling period, with a peak in local burning activities. During intensely biomass burning activities, ambient NO<sub>x</sub> ambient level reached a maximum of 421.2 ppb (58.4 ± 61.9). Moreover, the CO showed peak level at similar periods as NO<sub>x</sub>, and its concentration varied from 0.0 to 7.66 ppm (0.58 ± 0.79), as shown in figure S5. The diurnal variation of trace gases is shown in figure 2 (f, g, h, and i). The CO and NO<sub>x</sub> concentrations showed two peaks in days (06:00-08:00 and 17:00-20:00), attributed to the morning local biomass/trash burning emissions, night-time ...

**Supprimé:** current

**Supprimé:** said

**Supprimé:** NR-PM<sub>1</sub> (

**Supprimé:** )

**Supprimé:** f

**Supprimé:** ure

**Supprimé:** It means that a substantial mass of PM<sub>1</sub> was composed with non-refractory material and other refractory material like black carbon, metals and crustal material, whi...

**Supprimé:** OA was

**Supprimé:** with an average mass concentration of 46.5 ± 39.6 µg/m<sup>3</sup>

**Supprimé:** present

**Supprimé:** C

500 conducted at the current site (Gani et al., 2019; Rai et al., 2020). Campaign average mass concentration of  $\text{NO}_3^-$   
501 was  $10.1 \pm 7.0 \mu\text{g}/\text{m}^3$  and showed diurnal variation with a peak in the morning and midnight (Fig. 3(l)). Besides,  
502  $\text{SO}_4^{2-}$  showed slight enhancement at 08:00 hr and remained nearly constant from noon to 17:00 hr (Fig. 3(m)).  
503 However,  $\text{Cl}^-$  varied between 0.13 to  $77.83 \mu\text{g}/\text{m}^3$ , and higher concentrations of  $\text{Cl}^-$  were found episodic throughout  
504 the campaign. The  $\text{Cl}^-$  concentration was found consistent with Gani et al., 2019's previously reported value of  
505  $0.1\text{--}66.6 \mu\text{g}/\text{m}^3$  at the same site. The temporal variation of various OA factors is presented in Fig. 2(g and h).  
506 Biomass burning organic aerosol (BBOA) mass concentration peaks during the night and morning hours (Fig.  
507 3(r)). Low-volatility oxygenated organic aerosol (LO-OOA) exhibits a peak in the morning and remains relatively  
508 constant at noontime, suggesting steady formation. Meanwhile, moderately oxygenated organic aerosol (MO-  
509 OOA) shows a slight increase around noontime, indicating formation through daytime photooxidation (Mandariya  
510 et al., 2019; Sun et al., 2016). Overall, oxygenated organic aerosol (OOA) was the dominant fraction of OA during  
511 the sampling period. The H-BB events displayed a dynamic variation in BBOA mass concentration, ranging from  
512 16.3 to 134.7 (averaging  $50.7 \pm 24.0 \mu\text{g}/\text{m}^3$ ). Concurrently, these events also exhibited a higher concentration of  
513 HOA (ranging from 9.6 to  $109.4 \mu\text{g}/\text{m}^3$ ), suggesting a potential similarity in the sources of HOA during this  
514 occurrence. However, during H-HOA events, a higher concentration of HOA (ranging from 4.8 to  $58.9 \mu\text{g}/\text{m}^3$ )  
515 was observed, although these concentrations were notably lower than those observed during H-BB events.  
516 Nevertheless, fractional mass contribution of HOA to OA was largest among all OA species. Furthermore, H-Cl  
517 events exhibited elevated concentrations of both primary organic aerosol HOA and BBOA. BBOA contributed  
518 approximately 40.0%, 21.1%, 32.5%, and 13.1% to OA during H-BB, H-HOA, H-Cl, and relatively clean events,  
519 respectively, suggesting diverse sources of BBOA. Moreover, during the H-HOA event, HOA's average  
520 contribution was the highest among all events, at 41.6%. Additionally, Cl's fractional mass contribution in  $\text{PM}_{2.5}$   
521 reached up to 44.9% during the H-Cl event, in contrast to 21.2% in H-BB events and 7.3% in H-HOA events.

Supprimé: f

Supprimé: ure

Supprimé: 2

Supprimé: f

Supprimé: ure

Supprimé: 2

Mis en forme : Exposant

Supprimé: current

Supprimé: Figure 1 shows t

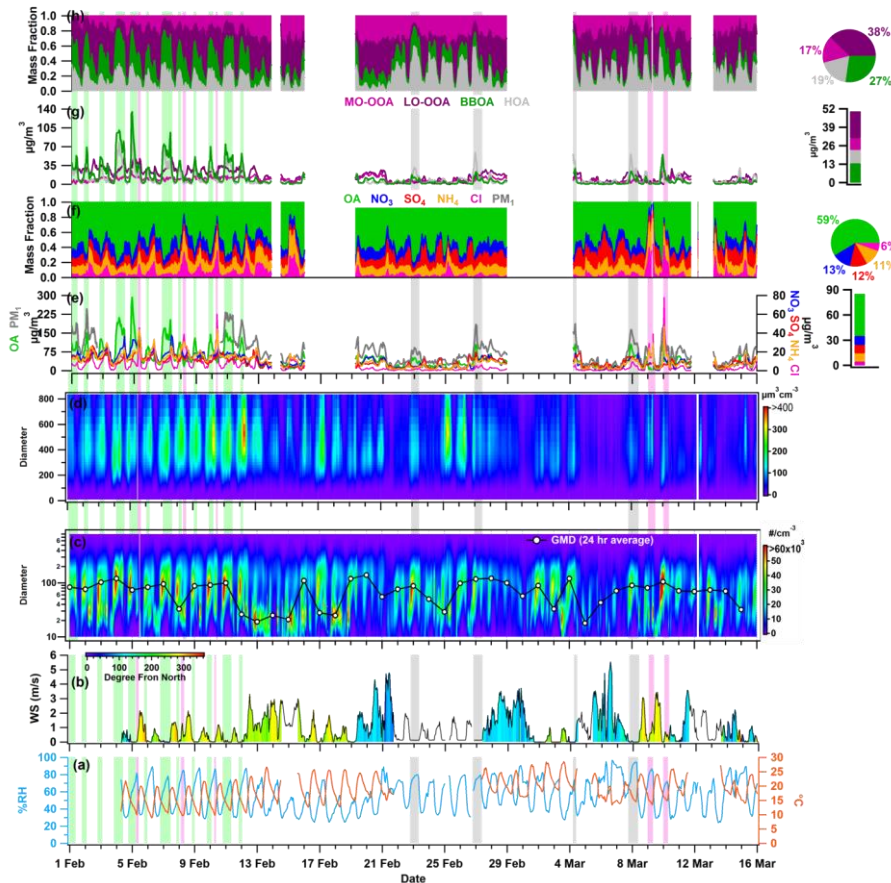
Mis en forme : Exposant

Mis en forme : Exposant

Mis en forme : Exposant

Mis en forme : Indice

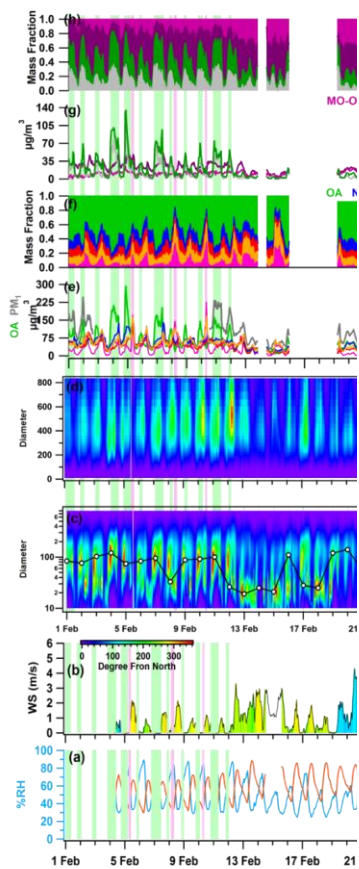
Supprimé: he temporal variation of all possible OA factors. BBOA mass concentration varied between 0.0 to 134.7  $\mu\text{g}/\text{m}^3$ . The two peaks during the night (21:00-23:00 hr) and morning (07:00-08:00 hr) featured the BBOA diurnal variation (figure 2(r)). Besides, LO-OOA diurnal variation peaked in the morning (10:00 hr) and remained nearly flattered at noontime. It could indicate its steady formation rate. However, the diurnal variation of MO-OOA showed a slight bump during noontime, indicating its formation via daytime photooxidation (Mandariya et al., 2019; Sun et al., 2016). Overall, oxygenated organic aerosol (OOA) was the dominant fraction of OA during the sampling period. Furthermore, based on the variability in aerosol chemical composition, three different events were observed: first, high-residential or local biomass burning (H-BB), second, high-hydrocarbon like OA (H-HOA), and third, high-chloride (H-Cl) period, characterized by high BBOA, HOA, and Cl, respectively. In addition, we also classified a "Clean Period" where  $\text{PM}_{2.5}$  loading was less than 25 percentile ( $\leq 38.7 \mu\text{g}/\text{m}^3$ ) of the sampling period. H-BB events showed a dynamic variation in BBOA mass concentration from 16.3 to 134.7 ( $50.7 \pm 24.0 \mu\text{g}/\text{m}^3$ ). Although, a higher mass concentration of HOA ( $9.6\text{--}109.4 \mu\text{g}/\text{m}^3$ ) was also observed in these events. It indicates that HOA also has probably similar sources during this event. Nevertheless, a higher HOA concentration ( $4.8\text{--}58.9 \mu\text{g}/\text{m}^3$ ) was noted during H-HOA events, although these concentrations were significantly lower than those observed during H-BB events. Nevertheless, fractional mass contribution of HOA to OA was largest among all OA species. Besides, H-Cl events observed a higher concentration of both primary organic aerosol HOA and BBOA. BBOA contributed nearly 40.0, 21.1, 32.5, and 13.1% to OA during H-BB, H-HOA, H-Cl, and relatively clean events, respectively, indicating different BBOA sources. Besides, the HOA's average contribution of 41.6% was observed in the H-HOA event was the highest among all events. In addition, Cl's fractional mass contribution in  $\text{PM}_{2.5}$  reached up to 44.9% in the H-Cl event compared to 21.2% (H-BB) and 7.3% (H-HOA) events.



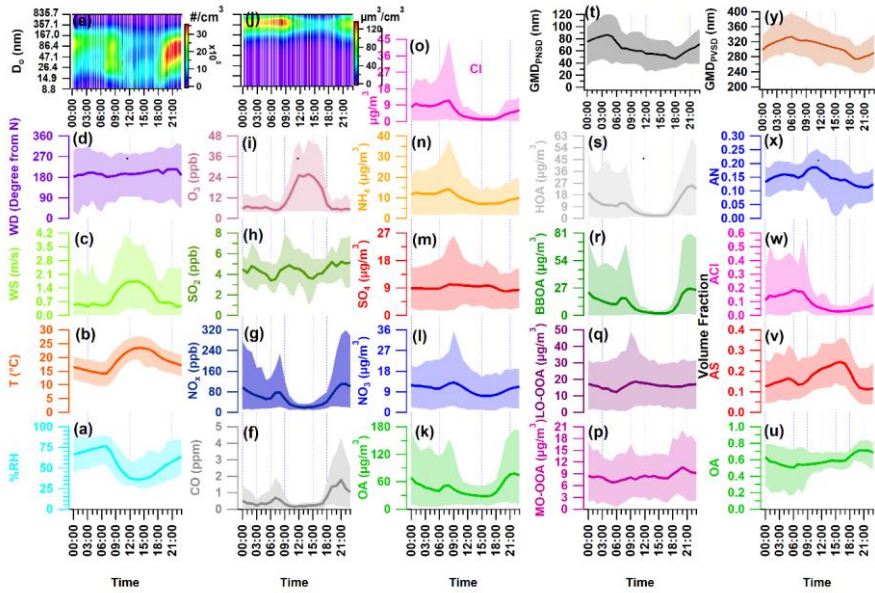
569

Supprimé:

570 Figure 2: Temporal variability of ambient (a) relative humidity (RH), temperature (T), (b) wind speed (WS), wind  
 571 direction (WD), (c) particle number-size distribution (PNSD), 24-average geometric mean diameter (GMD), (d) particle  
 572 volume-size distribution (PVSD), (e) particulate matter (PM<sub>1</sub>), organic aerosol (OA), nitrate (NO<sub>3</sub>), sulfate (SO<sub>4</sub>),  
 573 ammonium (NH<sub>4</sub>), chloride (Cl), (f) fractional contribution of OA, NO<sub>3</sub>, SO<sub>4</sub>, NH<sub>4</sub>, and Cl in PM<sub>1</sub>, (g) more oxidized-  
 574 oxygenated OA (MO-OOA), less oxidized-oxygenated OA (LO-OOA), biomass burning OA (BBOA), hydrocarbon like-  
 575 OA (HOA), and (h) fractional contribution of MO-OOA, LO-OOA, BBOA, and HOA in OA. The pie chart sub-plot  
 576 represents the overall average contribution of species, and the bar sub-plot represents the overall campaign average  
 577 value of different species. All other species are represented with specific color coding mentioned in legends. The light  
 578 green, pink, and grey color shaded vertical line indicates the high-BBOA (H-BBOA), high-HOA (H-HOA), and high-Cl  
 579 (H-Cl) events, respectively. The discontinuity in the data points marks the missing data or non-sampling time.



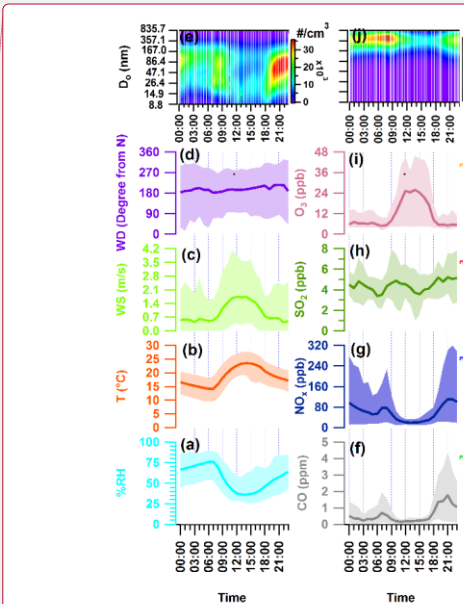
Supprimé:



584 **Figure 3:** Diurnal variation of ambient meteorological parameters (a) % ambient relative humidity (RH), (b)  
585 temperature (T), (c) wind speed (WS), (d) wind direction (WD), and (e) particle number size distribution (PNSD), mass  
586 concentration of ambient trace gases (f) carbon mono-oxide (CO), (g) nitrogen oxides (NOx), (h) sulfur dioxide (SO<sub>2</sub>),  
587 and (i) ozone (O<sub>3</sub>), (j) particle volume size distribution (PVSD), mass concentration of aerosol constituents (k) organic  
588 aerosol (OA), (l) nitrate (NO<sub>3</sub>), (m) sulfate (SO<sub>4</sub>), (n) ammonia (NH<sub>4</sub>), and (o) chloride (Cl), mass concentration of  
589 organic aerosol species (p) more oxidized-oxygenated OA (MO-OOA), (q) less oxidized-oxygenated OA (LO-OOA), (r)  
590 biomass burning OA (BBOA), and (s) hydrocarbon like-OA (HOA), (t) geometric mean diameter of particle number  
591 size distribution (GMD<sub>PNSD</sub>) and volume fractional contribution of (u) organic aerosol (OA), (v) ammonium sulfate  
592 (AS), (w) ammonium chloride (ACl), and (x) ammonium nitrate (AN) in PM<sub>1</sub>, and (y) geometric mean diameter of  
593 particle volume size distribution (GMD<sub>PVSD</sub>). Upper and lower boundary of shaded area represents the 95<sup>th</sup> and 5<sup>th</sup>  
594 percentile values of respective species.

595 **3.2 Hygroscopicity of Nucleation, Aitken, and Accumulation Mode Particles**

596 **3.2.1 Temporal variability**



Supprimé:

Supprimé: 2

599 Fig. 4 shows the dynamic variability in the hourly averaged HGF<sub>90%</sub> and hygroscopicity parameter ( $\kappa_{H-TDMA, 90\%}$ ,  
600 kappa) of Nucleation, Aitken, and Accumulation mode aerosol particles at 90% ambient relative humidity. The  
601 hygroscopic growth factors of 20 (HGF<sub>90%\_20nm</sub>), 50 (HGF<sub>90%\_50nm</sub>), 100 (HGF<sub>90%\_100nm</sub>), 150 (HGF<sub>90%\_150nm</sub>), and  
602 200 nm (HGF<sub>90%\_200nm</sub>) size particles varied between 1.00-1.41, 1.05-1.39, 1.11-1.49, 1.12-1.63, and 1.12-1.79  
603 with an average of  $1.14 \pm 0.09$  (average  $\pm$  standard deviation),  $1.16 \pm 0.06$ ,  $1.27 \pm 0.07$ ,  $1.35 \pm 0.09$ , and  $1.41 \pm$   
604 0.09, respectively. These mean hygroscopic growth factors were noted as statistically ( $p < 0.05$ ) different from each  
605 other. In addition, the hygroscopicity ( $\kappa_{20nm, 90\%}$  and  $\kappa_{50nm, 90\%}$ ) of 20 and 50 nm aerosol particles varied between  
606 0.00-0.11 and 0.02-0.25, with an average of  $0.03 \pm 0.02$  and  $0.09 \pm 0.03$ , respectively. Nucleation mode particles  
607 were observed, mainly monomodal GF-PDF (Fig. 4(a)), comprising nearly  $74 \pm 24\%$  nearly hydrophobic particles  
608 (HGF < 1.2). However, this contribution was raised to 100%, which was observed to have a good association with  
609 night-time local burning activities, as shown in the Fig. 4(a). The nucleation mode particles ( $\kappa_{20nm, 90\%}$ ) showed  
610 significantly ( $p < 0.05$ ) lower hygroscopicity than Aitken mode particles ( $\kappa_{50nm, 90\%}$ ). Hong et al. (2015) reported  
611 that nucleation mode particles are more sensitive to condensable vapors like fresh VOCs, H<sub>2</sub>SO<sub>4</sub> and HCl.  
612 However, the present study did not measure these species. The  $\kappa$  of Aitken size particles were comparable with  
613  $0.24 \pm 0.08$  of  $52.6 \pm 6.9$  size particles reported by Gunthe et al. (2011) for Beijing. Beijing is also one of the most  
614 polluted urban locations like Delhi, which could justify the comparison. However, Gunthe et al. (2011) performed  
615 this study using CCN on supersaturation levels. The campaign average hygroscopicity parameter (kappa,  $\kappa_{90\%}$ )  
616 increased significantly ( $p < 0.05$ ) with particle size, which can be attributed to the kelvin effect (Wang et al., 2018a).  
617 In the accumulation size range (100, 150, and 200 nm),  $\kappa_{90\%}$  increased to  $\sim 0.56$ . The overall sampling average  
618 values of  $\kappa_{100nm, 90\%}$ ,  $\kappa_{150nm, 90\%}$ , and  $\kappa_{200nm, 90\%}$  were  $0.14 \pm 0.04$ ,  $0.18 \pm 0.06$ , and  $0.22 \pm 0.07$ , respectively. The  
619  $\kappa_{200nm, 90\%}$  varied between 0.05 and 0.56. The similar kind of variation in  $\kappa$  with particle size has been demonstrated  
620 in Kanpur, situated at the center of IGP, India (Mandariya et al., 2020a) and worldwide studies (Cerully et al.,  
621 2015; Enroth et al., 2018; Fan et al., 2020; Kawana et al., 2016; Kim et al., 2020; Kitamori et al., 2009; Ogawa et  
622 al., 2016; Sjogren et al., 2012; Wang et al., 2018a). Moreover, this was attributed to the predominant increment  
623 in inorganic to OA fraction in particles with increment in size. Furthermore,  $\kappa_{H-TDMA, 90\%}$  was found approximately  
624 in the 0.13-0.77, reported by Arub et al. (2020) at Delhi for PM<sub>1</sub> without considering BC. Although, Arub et al.  
625 (2020) theoretically predicted particles' hygroscopicity by considering a particle's chemical composition. They  
626 found a decrease in  $\kappa$  calculation by 10% when BC was considered in aerosol chemical composition. Also,  $\kappa_{H-TDMA, 90\%}$   
627 measured in the current study were found in line with the global average value of  $0.27 \pm 0.21$  for  
628 continental aerosols (Petters and Kreidenweis, 2007; Pringle et al., 2010). Further, to understand the impact of a

Supprimé: ure

Supprimé: 3

Supprimé: 1

Supprimé: figure

Supprimé: 3

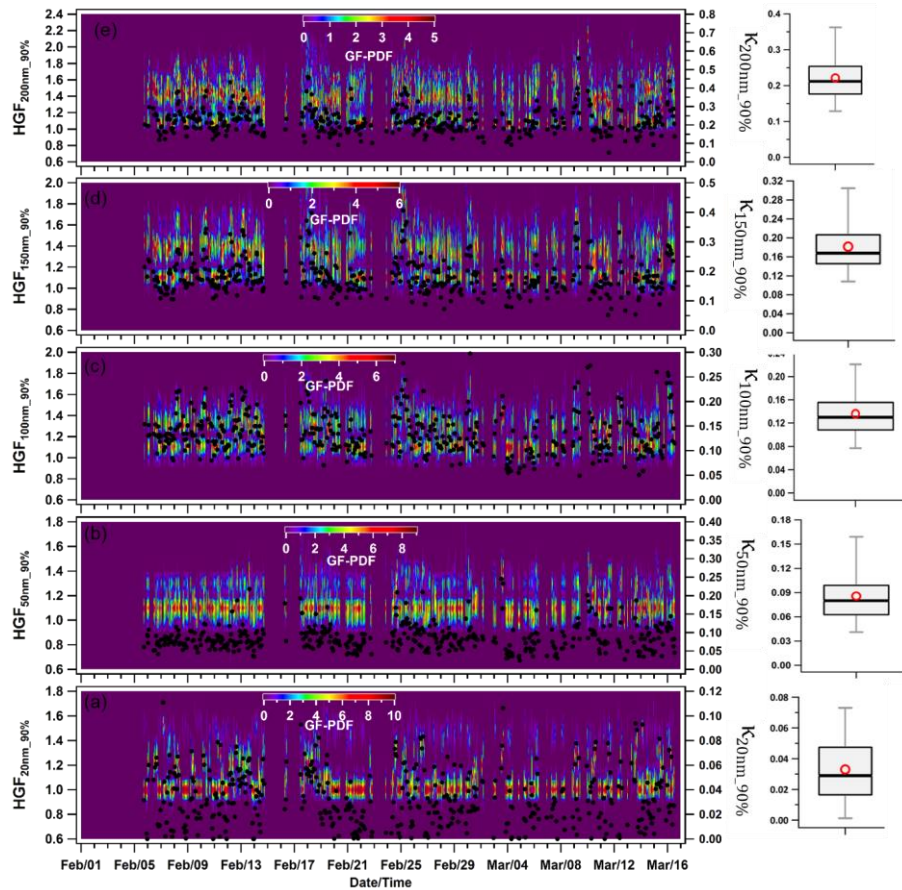
Supprimé: f

Supprimé: ure

Supprimé: 3

637 particle's chemical composition, local meteorology, and air mass trajectories on  $\kappa_{\text{H-TDMA,90\%}}$  for accumulation  
 638 mode particle discussed in subsequent sections.

639



640

641 **Figure 4:** Temporal variability in hygroscopic parameter kappa ( $\kappa$ ) of nucleation mode particles (a) 20 nm ( $\kappa_{20\text{nm},90\%}$ ),  
 642 Aitken mode particles (b) 50 nm ( $\kappa_{50\text{nm},90\%}$ ), and Accumulation mode particles (c) 100 nm ( $\kappa_{100\text{nm},90\%}$ ), (d) 150 nm  
 643 ( $\kappa_{150\text{nm},90\%}$ ), and (e) 200 nm ( $\kappa_{200\text{nm},90\%}$ ). The box plots represent the variability in the hygroscopicity of respective sizes  
 644 of particles in which low and high whisker traces represent the 5 and 95 percentile, respectively. The red marker  
 645 indicates the average of the data, whereas the upper and lower sides of the boxes indicate the 75 and 25 percentile of  
 646 the data, respectively.

Supprimé: 3

648 **3.2.2 Diurnal variability**

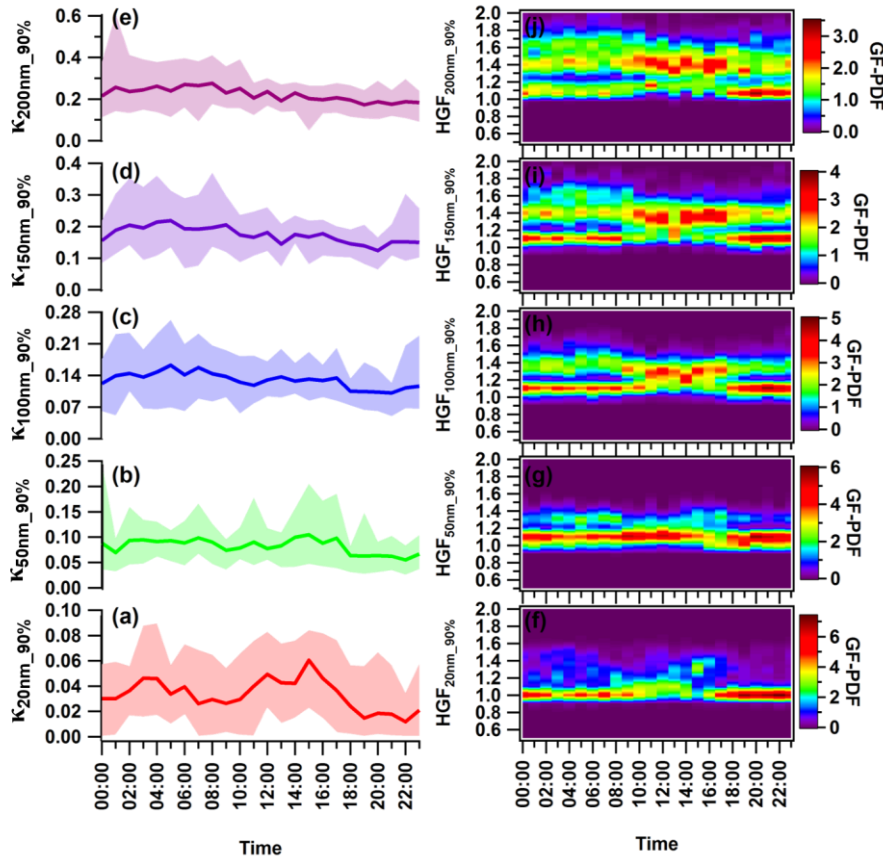
649 The diurnal variability in  $\kappa_{\text{H-TDMA,90\%}}$  was found different for nucleation ( $\kappa_{20\text{nm,90\%}}$ ), Aitken ( $\kappa_{50\text{nm,90\%}}$ ), and  
650 Accumulation ( $\kappa_{100\text{nm,90\%}}$ ,  $\kappa_{150\text{nm,90\%}}$ , and  $\kappa_{200\text{nm,90\%}}$ ) mode particles. Fig. 5 displayed a diel variation of an average  
651 of hourly-resolved  $\kappa$  for each size. The bigger size particles exhibited higher values of  $\kappa$  than smaller size particles,  
652 which is a similar trend reported at Kanpur, India (Mandariya et al., 2020a) and other worldwide locations (Fan  
653 et al., 2020; Hong et al., 2015). In general, it was observed that all size particles exhibited late-night hump (02:00-  
654 05:00 hr) in  $\kappa_{\text{H-TDMA,90\%}}$ . Besides, only  $\kappa_{20\text{nm,90\%}}$  demonstrated a clear diurnal variability with two peaks, one late  
655 night (02:00-04:00 hr) and the other in noontime (14:00-16:00 hr), and two valleys during the morning (07:00-  
656 10:00 hr) and night (19:00-22:00 hr). These valleys reflects the strong impacts of local burning and traffic  
657 activities (Pringle et al., 2010). In addition, nucleation size particles were potentially contributed by nearly  
658 hydrophobic particles (HGF<1.2) from evening to midnight. They showed mono modal GF-PDF around unit  
659 hygroscopic growth factor, possibly indicating local emission generated particles. The 20 nm particles are small  
660 enough and lie on the boundary of nucleation mode particles. Achtert et al. (2009) reported a similar diurnal trend  
661 of Nucleation and Aitken mode particles, attributed the lower values to the emission of hydrophobic aerosol  
662 particles during the local burning emissions. Daytime hump is attributed to the intense photochemical oxidation  
663 process, which causes the enhancement of more oxidized species on the aerosol particle. Furthermore, their  
664 chemical composition is dominantly controlled by the gaseous condensation of  $\text{H}_2\text{SO}_4$ ,  $\text{HNO}_3$ , and VOCs (Hong  
665 et al., 2015). The aerosol's chemical composition can address this variability of  $\kappa_{\text{H-TDMA,90\%}}$ . However,  $\kappa_{50\text{nm,90\%}}$   
666 also follows a similar diurnal variability as  $\kappa_{20\text{nm,90\%}}$ , although it showed less variability. Further, as the dry size  
667 of the aerosol particles increased to accumulated mode, diurnal variation shifted toward nearly steady for the rest  
668 of the day. Hong et al. (2018) also observed no obvious diurnal pattern for 100 and 150 nm particles of organic-  
669 dominated aerosols over the Pearl River Delta region in China.

670 Furthermore, the diurnal cycles of aerosol physicochemical properties also reflect the dynamic diurnal variation  
671 in the planetary boundary layer (PBL) that leads to the accumulation of particles during night-time. Although this  
672 study did not quantify size-resolved chemical composition, so, this study used bulk-aerosol composition to address  
673 the trend variability only. However, daily average aerosol PNSD varied between 18.0-140.0 nm with a mean of  
674  $73.1 \pm 33.8$  nm. And, the mode of PVSD changed approximately around 300-600 nm. Therefore, it could be an  
675 excellent approximation to discuss  $\kappa_{200\text{nm,90\%}}$  variability with aerosol's bulk chemical properties. The midnight to  
676 early morning hump in hygroscopicity of accumulation mode particles can be attributed to the high rise in the  
677 ratio of inorganic volume fraction to OA volume fraction (Fan et al., 2020), as illustrated in figure 2 (r, s t, u, and

Supprimé: ure  
Supprimé: 4

680 v). Moreover, during mid-night and early morning in the winter, water-soluble organic and inorganic gases are  
681 partitioned and/or coagulated/condensed on the surface of the pre-existing particles. Further, in the presence of  
682 high RH and lower temperature, primary and secondary less oxidized organic aerosol participated in the aging  
683 process, which leads to enhancement their oxidation via aqueous/heterogeneous reaction, according to it increase  
684 the particle's hygroscopicity (Jimenez et al., 2009; Wu et al., 2016). Similar results were observed by Fan et al.  
685 (2020) during winter in urban Beijing, and they attributed it with the enhancement of more hygroscopic particles  
686 due to the aqueous-oxidation and/or condensation process on the pre-existing particles. In general, higher  
687 noontime solar radiation ~~favours~~ more intense photooxidation processes. It supports the partitioning of relatively  
688 more oxidized and less volatile organics on the particulate surface, enhancing the hygroscopicity of accumulation  
689 mode particles (Duplissy et al., 2011; Massoli et al., 2010; Tritscher et al., 2011). However, interestingly, we  
690 observed a noontime flatten pattern of  $\kappa_{\text{H-TDMA,90\%}}$ , and it could be attributed to the mix of the positive and negative  
691 impact of an enhancement in the volume fraction of OA and more hygroscopic ammonium sulfate and decrement  
692 in ACl, and AN's volume fraction. Lower volume fractional contribution of highly volatile ACl could be the  
693 potential factor that modulates accumulation mode particle's hygroscopicity. This can be supported by the strong  
694 correlation of  $\kappa_{\text{H-TDMA,90\%}}$  and volume fraction of ACl in that size particles ( $\varepsilon_{\text{ACl}}$ ).

**Supprimé:** favors



696

697 Figure 5: Diurnal variance in the hygroscopic parameter kappa ( $\kappa$ ) of nucleation mode particles (a) 20 nm ( $\kappa_{20\text{nm}, 90\%}$ ),  
 698 Aitken mode particles (b) 50 nm ( $\kappa_{50\text{nm}, 90\%}$ ), and Accumulation mode particles (c) 100 nm ( $\kappa_{100\text{nm}, 90\%}$ ), (d) 150 nm  
 699 ( $\kappa_{150\text{nm}, 90\%}$ ), and (e) 200 nm ( $\kappa_{200\text{nm}, 90\%}$ ) and hygroscopic growth factor of (f) 20 nm ( $\text{HGF}_{20\text{nm}, 90\%}$ ), (g) 50 nm  
 700 ( $\text{HGF}_{50\text{nm}, 90\%}$ ), (h) 100 nm ( $\text{HGF}_{100\text{nm}, 90\%}$ ), (i) 150 nm ( $\text{HGF}_{150\text{nm}, 90\%}$ ), and 200 nm ( $\text{HGF}_{200\text{nm}, 90\%}$ ) aerosol particles. The  
 701 solid line represents diurnal average values, and the upper and lower shaded area represents 95 and 5 percentile values  
 702 of corresponding average values. Different color coding has been used to represent various size-specific kappa values.  
 703 The color scale represents the growth factor probability density function of hygroscopic growth factor.

### 704 3.2.3 Driving Factor of Hygroscopicity

705 A correlation analysis was carried out between measured chemical species and aerosol to explore the factors  
 706 governing aerosol hygroscopicity, as shown in the Fig. 6. Organic aerosol was observed negatively impact  $\kappa$ ,

Supprimé: 4

Supprimé: f

Supprimé: ure

Supprimé: 5

711 explained by a negative correlation (Fig. S7(a)). This negative correlation of OA with  $\kappa$  is also observed in India  
712 (Bhattu et al., 2016; Mandariya et al., 2020b) and worldwide (Enroth et al., 2018; Hong et al., 2014; Kawana et  
713 al., 2016; Kitamori et al., 2009; Wang et al., 2018a; Wu et al., 2013a). This result indicates that primary  
714 constituents dominated the OA during high loading, considered nearly hydrophobic or less hygroscopic. In  
715 addition, the current study observed that an enhancement of 10% of OA by volume in 200 nm aerosol particles  
716 would be responsible for a 4% decrement in its hygroscopicity (Fig. S7(a)). Interestingly, ammonium sulfate and  
717 nitrate showed a positive but poor correlation with hygroscopicity (Fig. 7(b and c)). It could be due to sulfate and  
718 nitrate aerosol dominating the bigger particles (>200nm). However, a 10% enhancement of AS by volume was  
719 found to be responsible for the enhancement of hygroscopicity only by 1.6%. But if AS contribution increased in  
720 the aerosol composition, aerosol water-bound capacity was negatively impacted (Fig. S8b) Besides, Fig. 6(a)  
721 shown an increasing volume fraction of ACl in  $PM_1$  with an increase in aerosol hygroscopicity, and this strong  
722 positive correlation is responsible for an enhancement in  $\kappa$  by 4.2% over the increment of 10% ACl by  
723 volume, which was the highest among all chemical species. Further, ammonium chloride has a more significant  
724 water uptake potential (Chen et al., 2022; Zhao et al., 2020), which can be justified by the solid correlation of  
725 aerosol liquid water content (ALWC) with a mass fraction of ACl in  $PM_1$  as shown in Fig. 6(b). This indicates  
726 that particles with a more considerable ammonium chloride fraction uptake more water vapor, leading to higher  
727 hygroscopic aerosol particles. It is clear that the increases in ammonium chloride fraction enhanced aerosol liquid  
728 water content and led to higher hygroscopicity of aerosol particles. A Recent study in Delhi by Chen et al. (2022)  
729 unveils that ammonium chloride fraction in  $PM_1$  aerosol enormously enhances during the higher relative humidity  
730 conditions during the winter season due to the co-condensation of semivolatile ammonium chloride with water  
731 vapor on the particles and leads to enhance water uptake and lead severe winter haze in Delhi. The very high  
732 volume fractions (>30%) of ACl in atmospheric  $PM_1$  were observed episodic, suggesting a high fraction of Cl in  
733 the particle phase is strongly dependent on excess ammonia in the atmosphere. These results indicate that ammonia  
734 is the controlling factor for chloride partitioning in the particle phase, resulting in high aerosol water content under  
735 high RH and lower temperature conditions. As the ACl is strongly dependent on the RH and temperature.

Supprimé: f

Supprimé: ure

Supprimé: figure

Supprimé: f

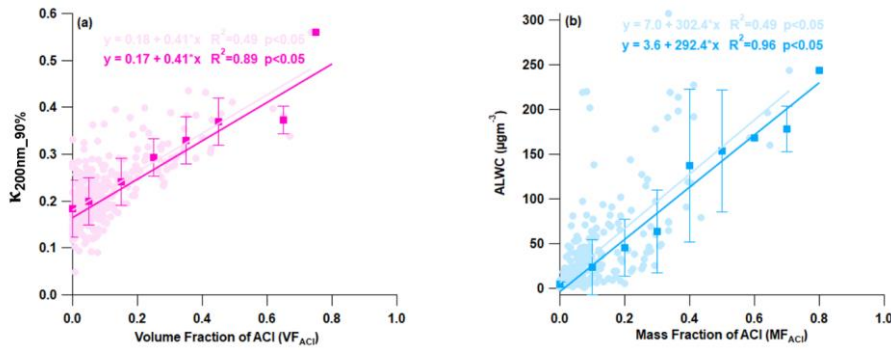
Supprimé: ure

Supprimé: 5

Supprimé: figure

Supprimé: 5

Supprimé: NR-



745

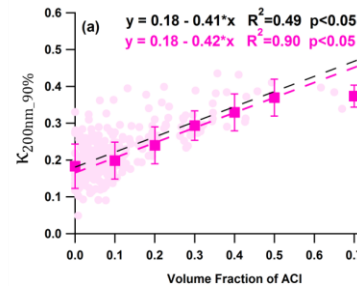
746 **Figure 6:** Correlation plot for (a)  $\kappa_{200\text{nm}, 90\%}$  vs volume fraction of ammonium chloride aerosol ( $\text{VF}_{\text{ACI}}$ ) and (b) aerosol  
747 liquid water content (ALWC) vs mass fraction of ammonium chloride ( $\text{MF}_{\text{ACI}}$ ). The solid circle and square marker  
748 represent the individual data points and the average of 10% volume and mass fraction increment of ACI data points,  
749 respectively. The light and dark color regression lines and equations indicate the overall and average (10% volume and  
750 mass fraction increment) correlation, respectively. The error bars indicate the standard deviation of the data points  
751 within the 10% mass and volume fractional bins.

752 **3.2.4 Hygroscopicity during high biomass burning (H-BB), high-hydrocarbon like OA (H-HOA), high-Cl  
753 (H-Cl), and relatively Clean Periods**

754 Delhi's atmosphere is a complex array of chloride and organic aerosol sources like combustion (crop residue,  
755 agriculture waste, medical waste, municipal waste, plastic, etc., burning) and industrial sources. Therefore, all  
756 episodic events were classified into three to investigate the impact of chloride and OA on aerosol hygroscopicity.  
757 First, high biomass burning (H-BB) event; second, high-hydrocarbon like OA (H-HOA) event; and third, high-Cl  
758 (H-Cl) events. Further, aerosol chemical composition data were filtered according to hygroscopic parameter data  
759 for further analysis. By performing so, data information that is characteristic of the local emission and atmospheric  
760 chemistry in question and the effects of various potential transported air mass types can be retrieved. It is valuable  
761 to extract any possible information about aerosol sources and transformation process evaluation to interpret its  
762 influence on the aerosol's hygroscopicity.

763 **3.2.4.1 High-Cl (H-Cl) events**

764 H-Cl events, representing the substantial loading of ACI on the receptor site, were chosen mainly due to the  
765 significant jump (>20%) in fractional volume contribution  $\text{NH}_4\text{Cl}$  ( $\varepsilon_{\text{ACI}}$ ) in the  $\text{PM}_1$  aerosol. This period observed  
766 apparent surface wind from W-direction, although WNW, WSW, and SE winds also influence the site, as shown



Supprimé:

**Supprimé: 5**

**Supprimé:** according to the substantial fractional contribution of their markers in respective periods. In addition, we also classified a "Clean Period" where  $\text{PM}_1$  loading was less than 25 percentile ( $\leq 38.7 \mu\text{g m}^{-3}$ ) of the sampling period.

**Supprimé: 3.2.4.1 Relatively Clean Period**

The relatively Clean period was predominantly dominated by E, S-E winds; however, pollution was associated with calm winds, as illustrated in figure S9. All BBOA, HOA, and ACI were observed to be associated with similar sources and found an excellent association with ambient relative humidity. The mean concentration of organic aerosol, ACI, AN, and AS was observed at  $11.0 \pm 6.4$ ,  $1.4 \pm 1.1$ ,  $3.0 \pm 1.5$ , and  $4.4 \pm 2.2 \mu\text{g m}^{-3}$ , respectively. These mass concentrations were significantly lower than in other specified periods. However, OA was still the dominant species, with 56% by volume in the  $\text{PM}_1$ , as indicated in figure 8. Among all OA factors, HOA was predominantly dominated in OA with 33%, although secondary organic aerosol confined the overall 54.4% of OA. Secondary OA is defined with relatively higher oxidized OA, and the oxidation state of OA positively impacts OA hygroscopicity (Kim et al., 2017; Richard et al., 2011; Wu et al., 2013a). The Clean period's mean hygroscopicity of 20, 50, 100, 150, and 200 nm particles were observed at  $0.03 \pm 0.02$ ,  $0.09 \pm 0.04$ ,  $0.14 \pm 0.06$ ,  $0.22 \pm 0.09$ , and  $0.27 \pm 0.07$ , respectively, significantly ( $p < 0.05$ ) different to each other. However, the accumulation particle's (200 nm) hygroscopicity was not significantly ( $p > 0.05$ ) higher than the 150 nm particles. The hygroscopicity increment with size from 20 to 200 nm can also be explained by the fractional increment of more hygroscopic ( $\text{GF} > 1.2$ ) particles relative to nearly hydrophobic or less hygroscopic particles ( $\text{GF} < 1.2$ ). Nucleation particles, 20 nm was dominated mostly by less hygroscopic particles ( $76.8 \pm 21.7\%$ ), indicates influence by fresh emission sources, whereas, Aitken (50 nm) and Accumulation (200 nm) size aerosol were confined with  $69.3 \pm 14.7$  and  $25.4 \pm 10.8$  less hygroscopic particles, respectively. These results point out that accumulation-size aerosols dominated secondary aerosols, which can also supports their GF-PDF as shown in figure 7(a). Nucleation size aerosol particles (20nm) showed nearly mono modal GF-PDF with the mode of unit growth factor. In contrast, the mode shifted towards the higher end as aerosol size increased and GF-PDF shifted from unit to multi-mode.¶

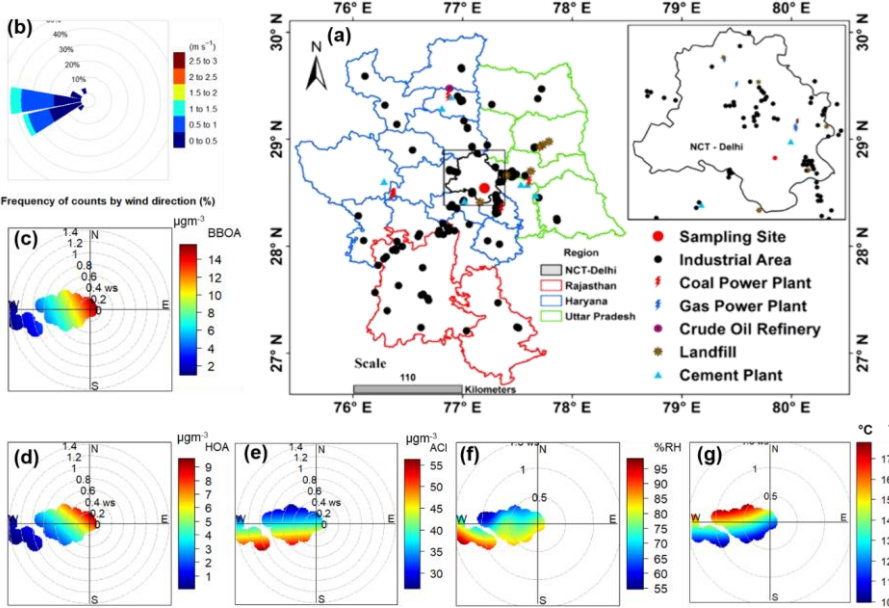
**Supprimé: 2**

**Supprimé:** as shown in the pie chart in figure 8,

815 in Fig. 7b. The average GMD of the PNSD was nearly 64 nm, indicating that local fresh emissions sources  
 816 influence the particles. In addition, the mean  $\text{SO}_2$ ,  $\text{NO}_x$ , and  $\text{CO}$  concentrations were at 3.6 ppb, 51.9 ppb, and 0.4  
 817 ppm, respectively. BBOA and HOA are potentially contributed from the WNW and SE directions, as explained  
 818 in the bipolar plot Fig. 7(c & d), and seem to come from a similar local source. Among inorganic species, ACI  
 819 observed excellent association with ambient RH, as shown in Fig. 7e and f, indicating the atmospheric gaseous  
 820  $\text{HCl}$  neutralized with  $\text{NH}_3$  gas in the presence of atmospheric water content.  $\text{HCl}$  sources could be coal power  
 821 plants, trash burnings in solid waste dumping sites, and other industries located in the W-WSW direction (Gani et  
 822 al., 2019), as shown in the map in Fig. 7a. Atmospheric high Cl events are potentially dominated by trash burning  
 823 in Delhi during winter (Shukla et al., 2021; Tobler et al., 2020). Moreover, bipolar plots (figure 6(e and f)) suggest  
 824 that ACI formation under high RH conditions associated with a relatively calm atmosphere trigger particles'  
 825 hygroscopicity. This hypothesis can be supported with a good association of aerosol liquid water content (ALWC)  
 826 as discussed in previous section. Furthermore, GF-PDF of all size particle marked relatively more fractionaly  
 827 contribution of secondary mode particles as showed in Fig. 8d. Overall more hygroscopic ( $\text{HGF90\%}>1.2$ )  
 828 particles were marked by 42, 47, 50, 74, and 83% contributions in the 20, 50, 100, 150, and 200 nm size particles,  
 829 respectively. Hence, ACI is a critical factor to enhance aerosol hygroscopicity to trigger fog/haze formation under  
 830 higher RH and colder atmospheric conditions as discussed in the previous section.  
 831 Similarly, Gunthe et al. (2021) observed that high local emission of hydrochloric acid in Delhi during February-  
 832 March gets partitions into aerosol liquid water under high humid conditions, enhancing the water uptake capacity  
 833 of aerosol sustain particle's hygroscopic growth, result in fog/haze formation. Moreover, worldwide studies on  
 834 size-resolved hygroscopicity observed Cl less than 1%, so they omitted ACI as an aerosol constituent into the  
 835 discussion. In addition, the current study did not find any strong correlation of  $\kappa$  with AS and AN. It could be due  
 836 to their association with larger particle sizes. Besides, ACI could be associated with comparatively lower size  
 837 particles ( $\leq 200$  nm). Furthermore, in context to look influence of air mass trajectories, we further mapped  
 838 aerosol's constituents in the association of air mass back trajectories in PSCF to see the potential area source  
 839 contribution influencing the aerosol evaluation processes, ultimately aerosol's hygroscopicity. However, we did  
 840 not find any back trajectory influencing the receptor site, as all trajectory endpoints were observed above the  
 841 planetary boundary layer height.

842

**Supprimé:** f  
**Supprimé:** ure  
**Supprimé:** 6(  
**Supprimé:** )  
**Mis en forme :** Indice  
**Supprimé:** figure  
**Supprimé:** 6  
**Supprimé:** f  
**Supprimé:** ure  
**Supprimé:** 6  
**Supprimé:** ( )  
**Supprimé:** ( )  
**Supprimé:** ( )  
**Supprimé:** f  
**Supprimé:** ure  
**Supprimé:** 6  
**Supprimé:** ( )  
**Supprimé:** f  
**Supprimé:** ure  
**Supprimé:** 7  
**Supprimé:** ( )  
**Supprimé:** )



866

867 **Figure 7** Map of (a) Delhi showing various types of industries located in the region and nearby locations, (b) wind rose  
 868 diagram and conditional bi-polar plots showing variation in mass concentration of (c) biomass burning OA (BBOA),  
 869 (d) hydrocarbon like OA (HOA), (e) ammonium chloride (ACI), (f) % ambient relative humidity (RH), and (g) ambient  
 870 temperature (T), with wind direction (WD) and wind speed (WS) during H-Cl events. A background map showing  
 871 various industrial locations was adapted from Rai et al. (2020).

872 **3.2.4.2 High biomass burning (H-BB) Events**

873 High BB events were noted during the initial period (1-12 February) of the field campaign. However, H-BB events  
 874 were generally captured either during the midnight (01:00 hours) to morning (08:00 hours) or evening (20:00  
 875 hours) to midnight (01:00 hours). Although, sometimes, it was continued from evening (21:00 hours) to morning  
 876 (11:00 hours). The predominant surface wind circulations were from W, W-WNW, and W-WSW directions (Fig.  
 877 S9b). The aerosol was dominated by local emissions, as aerosol constituents are mainly associated with slower  
 878 wind circulations from landfill sites, industrial areas, and coal power plants, as shown in Fig. S9a. Further, it could  
 879 justify the potential source contribution function (PSCF) analysis considering 48-hr air mass back trajectories, as  
 880 shown in Fig. S10. The average GMD of the PNSD was nearly 87 nm. In addition, the mean  $\text{SO}_2$ ,  $\text{NO}_x$ , and  $\text{CO}$   
 881 concentrations were at 4.7 ppb, 124.1 ppb, and 1.5 ppm, respectively. Therefore, BBOA possibly contributed from  
 882 the open local biomass burning activities at landfill sites or others. Organic aerosol in the H-BB event confined

Supprimé: 6

Supprimé: 3

Supprimé: periods

Supprimé: f

Supprimé: ure

Supprimé: 8(

Supprimé: )

Supprimé: f

Supprimé: ure

Supprimé: 8(

Supprimé: )

Supprimé: figure

Mis en forme : Indice

Supprimé: Biomass burning o

896 the most considerable fraction, 39%, of BBOA, following HOA, 28%. Figure S9, (b, c, and d) clearly shows that  
897 BBOA and HOA have similar local source profiles but differ from the ACI source. Moreover, ACI was not found  
898 to have a good association with ambient RH and but was associated with nearby coal power plant's emissions.  
899 However, 48 h air mass back trajectories indicated that the current city was also influenced by air mass from some  
900 parts of Uttar Pradesh, Punjab, and Haryana. These states are the potential hub of crop residue burning, industrial  
901 activities and brick kilns. These cities have a substantial fraction of OA in PM<sub>1</sub> and OA mainly affected by biomass  
902 activities during winter. The H-BB event captured a considerable volume fraction, 71% of OA in PM<sub>1</sub> and BBOA  
903 contributed almost 39%, as illustrated in the Fig. 9. So, lower inorganic to OA ratio was a potential factor in  
904 decreasing the aerosol hygroscopicity in H-BB events. Further, a primary organic aerosol contribution was  
905 enhanced during this event and, on average, raised to 67%. OA loading inversely affects the aerosol's  
906 hygroscopicity. Mandariya et al. (2020) reported a similar observation in Kanpur, and the authors suggested that  
907 the contribution of primary biomass burning (BBOA) and hydrocarbon-like OA adversely affects aerosol's  
908 hygroscopicity. BBOA showed a good negative correlation with the hygroscopicity of 200 nm particles,  
909 supporting the following conclusion. Apart from this, the Nucleation size particle (20 nm) showed  $0.02 \pm 0.02$   
910 hygroscopicity parameter with mono mode GF-PDF with the unit mode (Fig. 8b) and confined  $83.7 \pm 18.6$  %  
911 nearly hydrophobic particles. Furthermore, as aerosol size increased, hygroscopicity parameter ( $\kappa_{\text{H-TDMA}, 90\%}$ )  
912 enhanced significantly ( $p < 0.05$ ) as the contribution of relatively secondary aerosol particles ( $\text{GF} > 1.2$ ) increased  
913 with aerosol size. Accumulation size aerosol, 100 nm contributed approximately 54% by nearly hydrophobic  
914 ( $\text{GF} < 1.2$ ) and 46% by more hygroscopic ( $\text{GF} > 1.2$ ) particles.

### 915 3.2.4.3 High-HOA (H-HOA) Events

916 H-HOA events were identified based on the considerable mass concentration and fraction of HOA in the organic  
917 aerosol. These periods were noted generally 19:00 hr to Morning 09:00 hr during 22-23 and 26-27 February and  
918 4, and 7-8 March as indicated in Fig. 2. The average GMD of the PNSD was nearly 80 nm. In addition, the mean  
919  $\text{SO}_2$ ,  $\text{NO}_x$ , and  $\text{CO}$  concentrations were at 4.3 ppb, 136.7 ppb, and 1.1 ppm, respectively. PSCF explore the  
920 probability of impacts of long-range transported aerosol. Interestingly, it was observed that air masses over Delhi,  
921 Haryana, and Uttar Pradesh were potentially associated with hydrocarbon-like OA (Fig. S11). BBOA also  
922 followed a similar path as HOA. However, the potential area source of ACI was the nearby region of Delhi and  
923 Haryana. The HOA loading was significantly ( $p < 0.05$ ) higher than in H-BB, H-Cl and Clean periods. However,  
924 emission sources were different during both H-HOA and H-BB periods. As HOA was the potential contributor to  
925 OA, it is likely the critical constituent to modulate aerosol hygroscopicity in the region during these events. HOA

Supprimé: organic aerosol

Supprimé: 5

Supprimé: f

Supprimé: ure

Supprimé: 8

Supprimé: f

Supprimé: ure

Supprimé: 7(

Supprimé: )

Supprimé: 4

Supprimé: f

Supprimé: ure

Supprimé: 1

Supprimé: f

Supprimé: ure

Supprimé: 0

942 is mainly considered hydrophobic (Duplissy et al., 2011). Therefore, elevated HOA contribution (41%) in OA  
943 could be responsible for lower  $\kappa$  in these events. The overall hygroscopicity of 20, 50, 100, 150, and 200 nm size  
944 particles was recorded as  $0.01 \pm 0.01$ ,  $0.06 \pm 0.03$ ,  $0.11 \pm 0.03$ ,  $0.14 \pm 0.04$ , and  $0.17 \pm 0.05$ , respectively. The  
945 predominant fractional contribution of primary aerosol particles (GF<1.2) seems to be a reason for this lower  
946 hygroscopicity of particles, as shown in figure 7(c). Overall, OA predominantly constitutes the fraction in the  
947 PM<sub>1</sub>, and primary OA contributed approximately 60% in OA. However, relative increment in the contribution of  
948 other more hygroscopic constituents like secondary organic aerosol (LO-OOA and MO-OOA), ACI and  
949 ammonium sulfate (AS) in the aerosol possible tried to balance the negative impact high-HOA on which limited  
950  $\kappa$ .

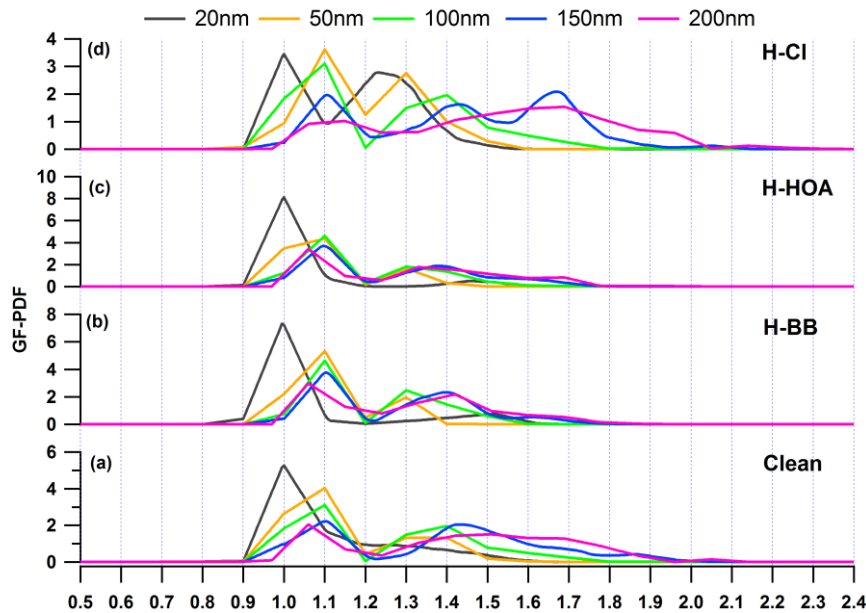
Supprimé:

#### 951 3.2.4.5 Relatively Clean Period

952 The 24<sup>th</sup> and 25<sup>th</sup> of February and the 5<sup>th</sup>, 6<sup>th</sup>, and 7<sup>th</sup> of March were marked as clean events. The night 21 hour to  
953 morning 11-hour duration was recorded as the clean duration. The relatively clean period was predominantly  
954 dominated by E, S-E winds; however, pollution was associated with calm winds, as illustrated in Fig. S9. The  
955 average GMD of the PNSD was nearly 54 nm. In addition, the mean SO<sub>2</sub>, NO<sub>x</sub>, and CO concentrations were at  
956 4.2 ppb, 43.2 ppb, and 0.4 ppm, respectively. All BBOA, HOA, and ACI were observed to be associated with  
957 similar sources and found an excellent association with ambient relative humidity. The mean concentration of  
958 organic aerosol, ACI, AN, and AS was observed at  $11.0 \pm 6.4$ ,  $1.4 \pm 1.1$ ,  $3.0 \pm 1.5$ , and  $4.4 \pm 2.2 \mu\text{gm}^{-3}$ ,  
959 respectively. These mass concentrations were significantly lower than in other specified periods. However, OA  
960 was still the dominant species, with 56% by volume in the PM<sub>1</sub>, as indicated in Fig. 9. Among all OA factors,  
961 HOA was predominantly dominated in OA with 33%, although secondary organic aerosol confined the overall  
962 54.4% of OA. Secondary OA is defined with relatively higher oxidized OA, and the oxidation state of OA  
963 positively impacts OA hygroscopicity (Kim et al., 2017; Richard et al., 2011; Wu et al., 2013a). The Clean period's  
964 mean hygroscopicity of 20, 50, 100, 150, and 200 nm particles were observed at  $0.03 \pm 0.02$ ,  $0.09 \pm 0.04$ ,  $0.14 \pm$   
965  $0.06$ ,  $0.22 \pm 0.09$ , and  $0.27 \pm 0.07$ , respectively, significantly (p<0.05) different to each other. However, the  
966 accumulation particle's (200 nm) hygroscopicity was not significantly (p>0.05) higher than the 150 nm particles.  
967 The hygroscopicity increment with size from 20 to 200 nm can also be explained by the fractional increment of  
968 more hygroscopic (GF>1.2) particles relative to nearly hydrophobic or less hygroscopic particles (GF<1.2).  
969 Nucleation particles, 20 nm was dominated mostly by less hygroscopic particles ( $76.8 \pm 21.7\%$ ), indicates  
970 influence by fresh emission sources, whereas, Aitken (50 nm) and Accumulation (200 nm) size aerosol were

972 confined with  $69.3 \pm 14.7$  and  $25.4 \pm 10.8$  less hygroscopic particles, respectively. These results point out that  
 973 accumulation-size aerosols dominated secondary aerosols, which can also support their GF-PDF as shown in Fig.  
 974 8(a). Nucleation size aerosol particles (20nm) showed nearly mono modal GF-PDF with the mode of unit growth  
 975 factor. In contrast, the mode shifted towards the higher end as aerosol size increased and GF-PDF shifted from  
 976 unit to multi-mode.

Mis en forme : Police :10 pt



977

978 Figure 8: Growth Factor Probability Density Function (GF-PDF) of 20, 50, 100, 150, and 200 nm aerosol particles for  
 979 the (a) clean, (b) H-BB, (c) H-HOA, and (d) H-Cl periods.

Supprimé: 7

#### 980 3.2.4.6 Comparison of $\kappa$ for different events

981 We considered a 200 nm accumulation particle size particle representing the bulk aerosol chemical composition  
 982 to compare the aerosol hygroscopicity among various periods. Further, in the present study, the mode of particle-  
 983 volume size distribution varied from 400 nm to 600 nm particle dry mobility diameter. Therefore, 200 nm size  
 984 accumulation particles are the best choice to compare hygroscopicity parameters among different periods  
 985 considering bulk aerosol composition in various mentioned periods. In addition, a good Pearson's r value, 0.76,

Supprimé: 4

Supprimé: of

Supprimé: hoose

990 was found among  $\kappa_{200\text{nm},90\%}$  and  $\kappa_{\text{chem},90\%}$ , derived from the dry PM<sub>1</sub> particle's chemical composition measured  
991 from the ACSM based on the ZSR mixing rule (Stokes and Robinson, 1966), which justifies our choice.

992 The H-Cl event noted the highest value ( $0.36 \pm 0.06$ ) of  $\kappa_{200\text{nm},90\%}$  against H-BB ( $0.18 \pm 0.04$ ), H-HOA ( $0.17 \pm$   
993  $0.05$ ), and Clean ( $0.27 \pm 0.07$ ) events, as illustrated in Fig. 9. The H-Cl event observed that the average  $\kappa_{200\text{nm},90\%}$   
994 value was significantly ( $p < 0.05$ ) higher than those observed in other events. It means that a substantial increment  
995 in Cl emission in the Delhi region could significantly enhance the aerosol liquid water content leading to higher  
996 aerosol hygroscopicity, which can further strengthen cloud condensation nuclei formation, possibly triggering  
997 haze/fog events in Delhi NCR (Gunthe et al., 2021). These results suggest that controlling the open trash/waste  
998 burning in the region could help control Cl emission, which leads to minimizing the haze/fog formation possibility  
999 during high atmospheric conditions. However, the difference in  $\kappa_{200\text{nm},90\%}$  values between H-BB and H-HOA  
1000 events was not observed significantly ( $p > 0.05$ ), possibly due to the relative changes in primary, secondary OA,  
1001 and inorganic species. In the H-HOA events, the negative effect of a significantly higher fractional (41%)  
1002 contribution of HOA to OA possibly balances with a positive impact of a 7% increment in secondary OA relative  
1003 to H-BB. Worldwide studies (Jimenez et al., 2009; Mandariya et al., 2019; Sun et al., 2013) reported secondary  
1004 organic aerosol associated with a higher O/C ratio, and several studies reported that the O/C ratio positively  
1005 correlated to  $\kappa$  (Jimenez et al., 2009; Kim et al., 2020) as described in the earlier text. Furthermore, impacts of  
1006 5% decrement in ACl during H-HOA event concerning H-BB event possibly managed by 7% increment in AS  
1007 fraction. Overall, these relative changes in aerosol constituents worked to insignificant changes in  $\kappa$  during H-BB  
1008 and H-HOA periods. Nevertheless, H-BB and H-HOA events witnessed significant ( $p < 0.05$ ) lower hygroscopicity  
1009 compared to a relatively cleaner atmosphere. The aerosol associated with relatively cleaner events was with a  
1010 higher inorganic-to-organic ratio. In addition, the aerosol in clean periods comprised a significantly higher fraction  
1011 of secondary organic aerosol, which could be the reason for the higher hygroscopicity associated with organic  
1012 aerosol compared to other events. Worldwide (Aiken et al., 2008; Cerully et al., 2015b; Chakraborty et al., 2016b;  
1013 Mandariya et al., 2019) studies have reported that organic aerosol loading inversely impacts the oxidation/aging  
1014 process of OA. Overall, all these were responsible for higher hygroscopicity in relatively cleaner periods.

Supprimé: f

Supprimé: ure

Supprimé: 8

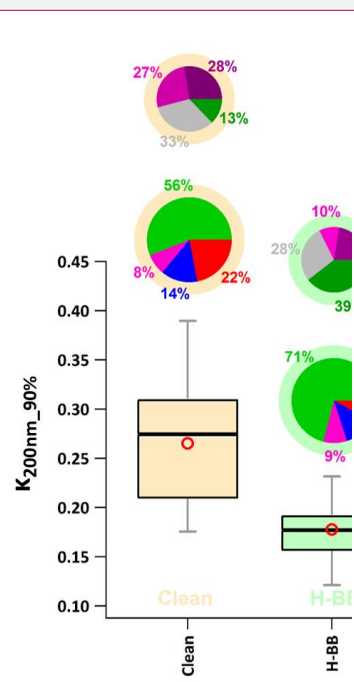
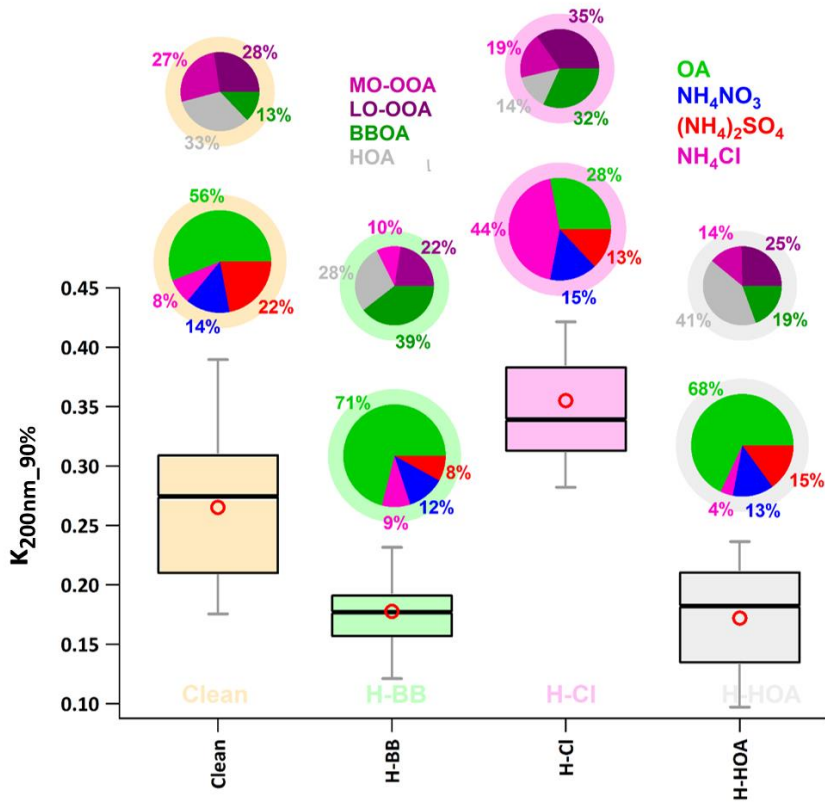


Figure 2: Box plot showing variation in H-TDMA measured hygroscopic parameter of 200 nm size particles ( $\kappa_{200\text{nm}}\text{-}_90\%$ ) in high biomass burning (H-BB), high-chloride (H-Cl), and high-hydrocarbon like organic aerosol (H-HOA) events. Different colors represent respective events in the plot. A bigger pie chart represents the overall average volume fractional contribution of various aerosol species indicated by color-coding. In addition, minor pie charts described the event average mass fractional contribution of different OA species in OA. Diffused ring color of the pie chart displays the respective event.

#### 4. Conclusions

The present study investigated the temporal variation of hygroscopicity in aerosol particles of different sizes, namely Nucleation (20 nm), Aitken (50 nm), and Accumulation (150 and 200 nm) modes in Delhi during the winter period of February-March 2020. This research also highlighted variations in hygroscopicity, specifically in aerosols with higher chloride, biomass burning, and hydrocarbon-like organic components. Delhi, known as

1033 one of the most polluted cities, often experiences high levels of chloride pollution during winter haze and fog  
1034 events. Consequently, this study reported the temporal variations in size-specific hygroscopic parameters ( $\kappa_{\text{H-TDMA, 90\%}}$ )  
1035 under sub-saturated conditions (90% RH) in Delhi for the first time. Furthermore, it presented the  
1036 hygroscopicity of nucleation and Aitken mode particles using HTDMA for the first time in India.  
1037 The observed  $\kappa_{\text{H-TDMA, 90\%}}$  values ranged from 0.00 to 0.11 (with an average of  $0.03 \pm 0.02$ ) for 20 nm aerosol  
1038 particles, 0.05 to 0.22 ( $0.11 \pm 0.03$ ) for 50 nm particles, 0.05 to 0.30 ( $0.14 \pm 0.04$ ) for 100 nm particles, 0.05 to  
1039 0.41 ( $0.18 \pm 0.06$ ) for 150 nm particles, and 0.05 to 0.56 ( $0.22 \pm 0.07$ ) for 200 nm particles. The average  
1040 hygroscopicity parameter for the study period significantly increased with the size of the particles ( $p < 0.05$ ).  
1041  $\kappa_{20\text{nm, 90\%}}$  and  $\kappa_{50\text{nm, 90\%}}$  displayed dynamic diurnal variations, while larger accumulation mode particles exhibited  
1042 a flatter diurnal pattern. This was attributed to the balancing positive and negative effects of changes in the volume  
1043 fraction of  $\text{NH}_4\text{Cl}$  and organic aerosol (OA) in the aerosol with increasing particle size. Interestingly, the variation  
1044 in  $\kappa_{200\text{nm, 90\%}}$  was primarily associated with fluctuations in  $\text{NH}_4\text{Cl}$  and OA, rather than  $(\text{NH}_4)_2\text{SO}_4$ .  
1045 Furthermore, pollution episodes were predominantly linked to local biomass burning and industrial and waste-  
1046 burning emissions in Delhi and nearby regions. The study primarily focused on highlighting the impacts of high  
1047 biomass burning (H-BB), high hydrocarbon-like OA (H-HOA), and high chloride emissions (H-Cl) on aerosol  
1048 hygroscopicity and compared them to cleaner periods. The H-Cl period exhibited significantly higher  
1049 hygroscopicity ( $0.35 \pm 0.06$ ) compared to H-BB ( $0.18 \pm 0.04$ ), H-HOA ( $0.17 \pm 0.05$ ), and the relatively cleaner  
1050 period ( $0.27 \pm 0.07$ ). However, H-BB and H-HOA showed no significant difference in hygroscopicity but  
1051 displayed lower hygroscopicity compared to cleaner periods. This could be attributed to lower organic aerosol  
1052 levels and a higher inorganic-to-organic aerosol ratio in the aerosol. The study also revealed that a 10% increase  
1053 in chloride aerosol (ammonium chloride) in the aerosol significantly enhanced hygroscopicity, leading to  
1054 approximately  $3 \mu\text{g m}^{-3}$  higher aerosol liquid water content during high chloride events. This 10% enhancement  
1055 of a high-volume fraction of ammonium chloride in aerosol enhanced the aerosol hygroscopicity significantly  
1056 ( $p < 0.05$ ) by 0.0041. Furthermore, the research suggested that chloride emissions were a significant concern in  
1057 Delhi, enhancing aerosol hygroscopicity, promoting cloud formation during winter days, and contributing to fog  
1058 and haze in the region. High chloride levels in aerosols counteracted the negative impact of high OA loading on  
1059 cloud condensation nuclei (CCN) activity. Consequently, the results indicated that controlling open burning of  
1060 waste materials could help reduce haze and fog events in Delhi during the winter months.

## 1061 Supporting Information

**Mis en forme** : Indice

**Mis en forme** : Exposant

**Supprimé:** The current study explored the temporal variation of Nucleation (20 nm), Aitken (50 nm), and Accumulation (150 and 200 nm) mode particle hygroscopicity in Delhi during the winter period, February–March 2020. In addition, the present study highlighted the hygroscopicity variation in relatively higher chloride, biomass burning, and hydrocarbon-like organic aerosol. Because, Delhi highlighted as one of the most polluted cities, faces high chloride pollution episodes during winter haze/fog. Therefore, we reported temporal variation in the size-resolved hygroscopic parameter ( $\kappa_{\text{H-TDMA, 90\%}}$ ) at the sub-saturated level (90% RH) for the first time in Delhi. However, we reported hygroscopicity of nucleation and Aitken mode particles for the first time in India.¶ The observed  $\kappa_{\text{H-TDMA, 90\%}}$  ranged from .00 to 0.11 ( $0.03 \pm 0.02$ ), 0.05 to 0.22 ( $0.11 \pm 0.03$ ), 0.05 to 0.30 ( $0.14 \pm 0.04$ ), 0.05 to 0.41 ( $0.18 \pm 0.06$ ), and 0.05 to 0.56 ( $0.22 \pm 0.07$ ) for 20, 50, 100, 150, and 200 nm aerosol particles, respectively. The study period's mean value of the hygroscopicity parameter was significantly ( $p < 0.05$ ) enhanced with the size of the particles.  $\kappa_{20\text{nm, 90\%}}$  and  $\kappa_{50\text{nm, 90\%}}$  were observed to show dynamic diurnal variation. In contrast, as particle size increased in accumulation mode particles, noontime variation became flatter, which found an attribute with neutralizing positive and negative impacts of increment and decrement in volume fraction of  $\text{NH}_4\text{Cl}$  and OA, respectively. Interestingly, the variation in  $\kappa_{200\text{nm, 90\%}}$  was observed potentially due to variation in  $\text{NH}_4\text{Cl}$  and OA instead  $(\text{NH}_4)_2\text{SO}_4$ .¶ Furthermore, the pollution episodes were generally associated with local biomass burning and industrial and waste-burning emissions in Delhi and nearby regions. We mainly focused on emphasizing the impacts of high biomass burning (H-BB), high hydrocarbons like OA (H-HOA), and high chloride emission (H-Cl) on aerosol hygroscopicity and their relative comparison with the cleaner period. The H-Cl period was observed significantly ( $p < 0.05$ ) higher hygroscopicity ( $0.35 \pm 0.06$ ) compared to H-BB ( $0.18 \pm 0.04$ ), H-HOA ( $0.17 \pm 0.05$ ), and relatively cleaner period ( $0.27 \pm 0.07$ ). However, H-BB and H-HOA showed no significant difference in hygroscopicity. However, they witnessed lower aerosol hygroscopicity concerning a relatively cleaner atmosphere. It could be attributed to the lower organic aerosol loading and higher inorganic-to-organic aerosol ratio in the aerosol. High atmospheric chloride aerosol (ammonium chloride) was observed most affectionately to the atmospheric water, leading to higher aerosol liquid water content at high chlori...

1167 Supplementary pieces of information are mentioned in the supplementary file.

1168 **Data availability.** Data can be accessed at the following repository:

1169 <https://web.iitd.ac.in/~gazala/publications.html> (Mandariya et al., 2023).

1170 **Author contributions**

1171 AH, MMVH, NAB, and GH operated aerosol instrumentation and collection of data on-board in Delhi. KP  
1172 analysed the ACSM data. AKM, AH, and GH conceptualized the structure of the manuscript. AKM analysed,  
1173 evaluated H-TDMA data, and wrote the manuscript. AH analysed MPSS data. AKM, AH, KP, JSA, LHR, AW,  
1174 and GH internally reviewed the manuscript and helped to write the manuscript.

1175 **Corresponding Author**

1176 Gazala Habib (gazalahabib@civil.iitd.ac.in) and Alfred Wiedensohler (ali@tropos.de)

1177 **Competing interests**

1178 The authors declare that they have no conflict of interest.

1179

1180 **Acknowledgment**

1181 The authors thankful to Dr. Martin Gysel, Aerosol Physics Group, Paul Scherrer Institute, Switzerland, for  
1182 providing TDMAinv toolkit for HTDMA data correction.

1183 **REFERENCES**

1184 Achtert, P., Birmili, W., Nowak, A., Wehner, B., Wiedensohler, A., Takegawa, N., Kondo, Y., Miyazaki, Y., Hu,  
1185 M. and Zhu, T.: Hygroscopic growth of tropospheric particle number size distributions over the North China Plain,  
1186 *J. Geophys. Res.*, 114(8), D00G07, doi:10.1029/2008JD010921, 2009.

1187 Aiken, A. C., Decarlo, P. F., Kroll, J. H., Worsnop, D. R., Huffman, J. A., Docherty, K. S., Ulbrich, I. M., Mohr,  
1188 C., Kimmel, J. R., Sueper, D., Sun, Y., Zhang, Q., Trimborn, A., Northway, M., Ziemann, P. J., Canagaratna, M.  
1189 R., Onasch, T. B., Alfarra, M. R., Prevot, A. S. H., Dommen, J., Duplissy, J., Metzger, A., Baltensperger, U. and  
1190 Jimenez, J. L.: O/C and OM/OC ratios of primary, secondary, and ambient organic aerosols with high-resolution  
1191 time-of-flight aerosol mass spectrometry, *Environ. Sci. Technol.*, 42(12), 4478–4485, doi:10.1021/es703009q,  
1192 2008.

1193 Albrecht, B. A.: Aerosols, Cloud Microphysics, and Fractional Cloudiness, *Science* (80-.), 245(4923), 1227–  
1194 1230, doi:10.1126/science.245.4923.1227, 1989.

1195 Arub, Z., Bhandari, S., Gani, S., Apte, J. S., Hildebrandt Ruiz, L. and Habib, G.: Air mass physiochemical  
1196 characteristics over New Delhi: impacts on aerosol hygroscopicity and cloud condensation nuclei (CCN)  
1197 formation, *Atmos. Chem. Phys.*, 20(11), 6953–6971, doi:10.5194/acp-20-6953-2020, 2020.

1198 Bhandari, S., Gani, S., Patel, K., Wang, D. S., Soni, P., Arub, Z., Habib, G., Apte, J. S. and Hildebrandt Ruiz, L.:  
1199 Sources and atmospheric dynamics of organic aerosol in New Delhi, India: insights from receptor modeling,  
1200 *Atmos. Chem. Phys.*, 20(2), 735–752, doi:10.5194/acp-20-735-2020, 2020.

1201 Bhattu, D. and Tripathi, S. N.: CCN closure study: Effects of aerosol chemical composition and mixing state, *J. Geophys. Res.*, 120(2), 766–783, doi:10.1002/2014JD021978, 2015.

1203 Bhattu, D., Tripathi, S. N. and Chakraborty, A.: Deriving aerosol hygroscopic mixing state from size-resolved  
1204 CCN activity and HR-ToF-AMS measurements, *Atmos. Environ.*, 142, 57–70,  
1205 doi:10.1016/j.atmosenv.2016.07.032, 2016.

1206 Cerulley, K. M., Bougiatioti, A., Hite, J. R., Guo, H., Xu, L., Ng, N. L., Weber, R. and Nenes, A.: On the link  
1207 between hygroscopicity, volatility, and oxidation state of ambient and water-soluble aerosols in the southeastern  
1208 United States, *Atmos. Chem. Phys.*, 15(15), 8679–8694, doi:10.5194/acp-15-8679-2015, 2015a.

1209 Cerulley, K. M., Bougiatioti, A., Hite, J. R., Guo, H., Xu, L., Ng, N. L., Weber, R. and Nenes, A.: On the link  
1210 between hygroscopicity, volatility, and oxidation state of ambient and water-soluble aerosols in the southeastern  
1211 United States, *Atmos. Chem. Phys.*, 15(15), 8679–8694, doi:10.5194/acp-15-8679-2015, 2015b.

1212 Chakraborty, A., Gupta, T. and Tripathi, S. N.: Combined effects of organic aerosol loading and fog processing  
1213 on organic aerosols oxidation, composition, and evolution, *Sci. Total Environ.*, 573, 690–698,  
1214 doi:10.1016/j.scitotenv.2016.08.156, 2016a.

1215 Chakraborty, A., Gupta, T. and Tripathi, S. N.: Combined effects of organic aerosol loading and fog processing  
1216 on organic aerosols oxidation, composition, and evolution, *Sci. Total Environ.*, 573, 690–698,  
1217 doi:10.1016/j.scitotenv.2016.08.156, 2016b.

1218 Chen, Y., Wang, Y., Nenes, A., Wild, O., Song, S., Hu, D., Liu, D., He, J., Hildebrandt Ruiz, L., Apte, J. S.,  
1219 Gunthe, S. S. and Liu, P.: Ammonium Chloride Associated Aerosol Liquid Water Enhances Haze in Delhi, India,  
1220 *Environ. Sci. Technol.*, 56(11), 7163–7173, doi:10.1021/ACS.EST.2C00650, 2022.

1221 Draxler, Roland R., Hess, G. D.: Description of the HYSPLIT\_4 Modeling System, NOAA Technical Memo.  
1222 ERL ARL-224, (October 2004), 28 [online] Available from: <http://arlsun.arlhq.noaa.gov/documents/reports/arlr-224.pdf> 5Cnhttp://www.ciemem.uhu.es/hysplitweb08/document/arlr-224.pdf, 1997.

1224 Duplissy, J., De Carlo, P. F., Dommen, J., Alfara, M. R., Metzger, A., Barmpadimos, I., Prevot, A. S. H.,  
1225 Weingartner, E., Tritscher, T., Gysel, M., Aiken, A. C., Jimenez, J. L., Canagaratna, M. R., Worsnop, D. R.,  
1226 Collins, D. R., Tomlinson, J. and Baltensperger, U.: Relating hygroscopicity and composition of organic aerosol  
1227 particulate matter, *Atmos. Chem. Phys.*, 11(3), 1155–1165, doi:10.5194/acp-11-1155-2011, 2011.

1228 Enroth, J., Mikkilä, J., Németh, Z., Kulmala, M. and Salma, I.: Wintertime hygroscopicity and volatility of  
1229 ambient urban aerosol particles, *Atmos. Chem. Phys.*, 18(7), 4533–4548, doi:10.5194/acp-18-4533-2018, 2018.

1230 Ervens, B., Turpin, B. J. and Weber, R. J.: Secondary organic aerosol formation in cloud droplets and aqueous  
1231 particles (aqSOA): A review of laboratory, field and model studies, *Atmos. Chem. Phys.*, 11(21), 11069–11102,  
1232 doi:10.5194/acp-11-11069-2011, 2011.

1233 Fan, X., Liu, J., Zhang, F., Chen, L., Collins, D., Xu, W., Jin, X., Ren, J., Wang, Y., Wu, H., Li, S., Sun, Y. and  
1234 Li, Z.: Contrasting size-resolved hygroscopicity of fine particles derived by HTDMA and HR-ToF-AMS  
1235 measurements between summer and winter in Beijing: the impacts of aerosol aging and local emissions, *Atmos.*  
1236 *Chem. Phys.*, 20(2), 915–929, doi:10.5194/acp-20-915-2020, 2020.

1237 Fountoukis, C. and Nenes, A.: ISORROPIAII: A computationally efficient thermodynamic equilibrium model for  
1238 K<sup>+</sup>-Ca<sup>2+</sup>-Mg<sup>2+</sup>-NH<sub>4</sub><sup>+</sup>-Na<sup>+</sup>-SO<sub>4</sub><sup>2-</sup>-NO<sub>3</sub><sup>-</sup>-Cl<sup>-</sup>-H<sub>2</sub>O aerosols, *Atmos. Chem. Phys.*, 7(17), 4639–4659,  
1239 doi:10.5194/acp-7-4639-2007, 2007.

1240 Gani, S., Bhandari, S., Seraj, S., Wang, D. S., Patel, K., Soni, P., Arub, Z., Habib, G., Hildebrandt Ruiz, L. and  
1241 Apte, J. S.: Submicron aerosol composition in the world's most polluted megacity: the Delhi Aerosol Supersite  
1242 study, *Atmos. Chem. Phys.*, 19(10), 6843–6859, doi:10.5194/acp-19-6843-2019, 2019.

1243 Gunthe, S. S., Rose, D., Su, H., Garland, R. M., Achtert, P., Nowak, A., Wiedensohler, A., Kuwata, M., Takegawa, N., Kondo, Y., Hu, M., Shao, M., Zhu, T., Andreae, M. O. and Pöschl, U.: Cloud condensation nuclei (CCN) from fresh and aged air pollution in the megacity region of Beijing, *Atmos. Chem. Phys.*, 11(21), 11023–11039, doi:10.5194/acp-11-11023-2011, 2011.

1247 Gunthe, S. S., Liu, P., Panda, U., Raj, S. S., Sharma, A., Darbyshire, E., Reyes-Villegas, E., Allan, J., Chen, Y., Wang, X., Song, S., Pöhlker, M. L., Shi, L., Wang, Y., Kommula, S. M., Liu, T., Ravikrishna, R., McFiggans, G., Mickley, L. J., Martin, S. T., Pöschl, U., Andreae, M. O. and Coe, H.: Enhanced aerosol particle growth sustained by high continental chlorine emission in India, *Nat. Geosci.*, 14(2), 77–84, doi:10.1038/s41561-020-00677-x, 2021.

1252 Gupta, T. and Mandariya, A.: Sources of submicron aerosol during fog-dominated wintertime at Kanpur, *Environ. Sci. Pollut. Res.*, 20(8), doi:10.1007/s11356-013-1580-6, 2013.

1254 Gysel, M., Crosier, J., Topping, D. O., Whitehead, J. D., Bower, K. N., Cubison, M. J., Williams, P. I., Flynn, M. J., McFiggans, G. B. and Coe, H.: Closure study between chemical composition and hygroscopic growth of aerosol particles during TORCH2, *Atmos. Chem. Phys.*, 7(24), 6131–6144, doi:10.5194/acp-7-6131-2007, 2007.

1257 Gysel, M., McFiggans, G. B. and Coe, H.: Inversion of tandem differential mobility analyser (TDMA) measurements, *J. Aerosol Sci.*, 40(2), 134–151, doi:10.1016/j.jaerosci.2008.07.013, 2009.

1259 Hallquist, M., Wenger, J. C., Baltensperger, U., Rudich, Y., Simpson, D., Claeys, M., Dommen, J., Donahue, N. M., George, C., Goldstein, A. H., Hamilton, J. F., Herrmann, H., Hoffmann, T., Linuma, Y., Jang, M., Jenkin, M. E., Jimenez, J. L., Kiendler-Scharr, A., Maenhaut, W., McFiggans, G., Mentel, T. F., Monod, A., Pfeifert, A. S. H., Seinfeld, J. H., Surratt, J. D., Szmigielski, R. and Wildt, J.: The formation, properties and impact of secondary organic aerosol: current and emerging issues, *Atmos. Chem. Phys.*, 9(November 2008), 5155–5236, 2009.

1264 Hong, J., Häkkinen, S. A. K., Paramonov, M., Äijälä, M., Hakala, J., Nieminen, T., Mikkilä, J., Prisle, N. L., Kulmala, M., Riipinen, I., Bilde, M., Kerminen, V. M. and Petäjä, T.: Hygroscopicity, CCN and volatility properties of submicron atmospheric aerosol in a boreal forest environment during the summer of 2010, *Atmos. Chem. Phys.*, 14(9), 4733–4748, doi:10.5194/acp-14-4733-2014, 2014.

1268 Hong, J., Kim, J., Nieminen, T., Duplissy, J., Ehn, M., Äijälä, M., Hao, L. Q., Nie, W., Sarnela, N., Prisle, N. L., Kulmala, M., Virtanen, A., Petäjä, T. and Kerminen, V. M.: Relating the hygroscopic properties of submicron aerosol to both gas- and particle-phase chemical composition in a boreal forest environment, *Atmos. Chem. Phys.*, 15(20), 11999–12009, doi:10.5194/acp-15-11999-2015, 2015.

1272 Hong, J., Xu, H., Tan, H., Yin, C., Hao, L., Li, F., Cai, M., Deng, X., Wang, N., Su, H., Cheng, Y., Wang, L., Petäjä, T. and Kerminen, V. M.: Mixing state and particle hygroscopicity of organic-dominated aerosols over the Pearl River Delta region in China, *Atmos. Chem. Phys.*, 18(19), 14079–14094, doi:10.5194/acp-18-14079-2018, 2018.

1276 Hu, D., Chen, J., Ye, X., Li, L. and Yang, X.: Hygroscopicity and evaporation of ammonium chloride and ammonium nitrate: Relative humidity and size effects on the growth factor, *Atmos. Environ.*, 45(14), 2349–2355, doi:10.1016/j.atmosenv.2011.02.024, 2011.

1279 Jimenez, J. L., Canagaratna, M. R., Donahue, N. M., Prevot, A. S. H., Zhang, Q., Kroll, J. H., DeCarlo, P. F., Allan, J. D., Coe, H., Ng, N. L., Aiken, A. C., Docherty, K. S., Ulbrich, I. M., Grieshop, A. P., Robinson, A. L., Duplissy, J., Smith, J. D., Wilson, K. R., Lanz, V. A., Hueglin, C., Sun, Y. L., Tian, J., Laaksonen, A., Raatikainen, T., Rautiainen, J., Vaattovaara, P., Ehn, M., Kulmala, M., Tomlinson, J. M., Collins, D. R., Cubison, M. J., Dunlea, E. J., Huffman, J. A., Onasch, T. B., Alfarra, M. R., Williams, P. I., Bower, K., Kondo, Y., Schneider, J., Drewnick, F., Borrmann, S., Weimer, S., Demerjian, K., Salcedo, D., Cottrell, L., Griffin, R., Takami, A., Miyoshi, T., Hatakeyama, S., Shimono, A., Sun, J. Y., Zhang, Y. M., Dzepina, K., Kimmel, J. R., Sueper, D., Jayne, J. T., Herndon, S. C., Trimborn, A. M., Williams, L. R., Wood, E. C., Middlebrook, A. M., Kolb, C. E., Baltensperger, U. and Worsnop, D. R.: Evolution of organic aerosols in the atmosphere, *Science* (80-), 326(5959), 1525–1529, doi:10.1126/science.1180353, 2009.

1289 Kawana, K., Nakayama, T. and Mochida, M.: Hygroscopicity and CCN activity of atmospheric aerosol particles and their relation to organics: Characteristics of urban aerosols in Nagoya, Japan, *J. Geophys. Res. Atmos.*, 121(8), 4100–4121, doi:10.1002/2015JD023213, 2016.

1292 Kecorius, S., Vogl, T., Paasonen, P., Lampilahti, J., Rothenberg, D., Wex, H., Zeppenfeld, S., Van Pinxteren, M.,  
1293 Hartmann, M., Henning, S., Gong, X., Welti, A., Kulmala, M., Stratmann, F., Herrmann, H. and Wiedensohler,  
1294 A.: New particle formation and its effect on cloud condensation nuclei abundance in the summer Arctic: a case  
1295 study in the Fram Strait and Barents Sea, *Atmos. Chem. Phys.*, 19, 14339–14364, doi:10.5194/acp-19-14339-2019,  
1296 2019.

1297 Kim, N., Park, M., Yum, S. S., Park, J. S., Song, I. H., Shin, H. J., Ahn, J. Y., Kwak, K. H., Kim, H., Bae, G. N.  
1298 and Lee, G.: Hygroscopic properties of urban aerosols and their cloud condensation nuclei activities measured in  
1299 Seoul during the MAPS-Seoul campaign, *Atmos. Environ.*, 153, 217–232, doi:10.1016/j.atmosenv.2017.01.034,  
1300 2017.

1301 Kim, N., Yum, S. S., Park, M., Park, J. S., Shin, H. J. and Ahn, J. Y.: Hygroscopicity of urban aerosols and its  
1302 link to size-resolved chemical composition during spring and summer in Seoul, Korea, *Atmos. Chem. Phys.*,  
1303 20(19), 11245–11262, doi:10.5194/acp-20-11245-2020, 2020.

1304 Kitamori, Y., Mochida, M. and Kawamura, K.: Assessment of the aerosol water content in urban atmospheric  
1305 particles by the hygroscopic growth measurements in Sapporo, Japan, *Atmos. Environ.*, 43(21), 3416–3423,  
1306 doi:10.1016/j.atmosenv.2009.03.037, 2009.

1307 Kroll, J. H., Donahue, N. M., Jimenez, J. L., Kessler, S. H., Canagaratna, M. R., Wilson, K. R., Altieri, K. E.,  
1308 Mazzoleni, L. R., Wozniak, A. S., Bluhm, H., Mysak, E. R., Smith, J. D., Kolb, C. E. and Worsnop, D. R.: Carbon  
1309 oxidation state as a metric for describing the chemistry of atmospheric organic aerosol, *Nat. Chem.*, 3(2), 133–  
1310 139, doi:10.1038/nchem.948, 2011.

1311 Li, H., Wang, Q., Shao, M., Wang, J., Wang, C., Sun, Y., Qian, X., Wu, H., Yang, M. and Li, F.: Fractionation of  
1312 airborne particulate-bound elements in haze-fog episode and associated health risks in a megacity of southeast  
1313 China, *Environ. Pollut.*, 208, 655–662, doi:10.1016/j.envpol.2015.10.042, 2016.

1314 Liu, J., Horowitz, L. W., Fan, S., Carlton, A. G. and Levy, H.: Global in-cloud production of secondary organic  
1315 aerosols: Implementation of a detailed chemical mechanism in the GFDL atmospheric model AM3, *J. Geophys.*  
1316 *Res. Atmos.*, 117(D15), n/a-n/a, doi:10.1029/2012JD017838, 2012.

1317 Lohmann, U. and Feichter, J.: Global indirect aerosol effects: a review, *Atmos. Chem. Phys.*, 5(3), 715–737,  
1318 doi:10.5194/acp-5-715-2005, 2005.

1319 Mandariya, A. K., Gupta, T. and Tripathi, S. N.: Effect of aqueous-phase processing on the formation and  
1320 evolution of organic aerosol (OA) under different stages of fog life cycles, *Atmos. Environ.*, 206(November 2018),  
1321 60–71, doi:10.1016/j.atmosenv.2019.02.047, 2019.

1322 Mandariya, A. K., Tripathi, S. N., Gupta, T. and Mishra, G.: Wintertime hygroscopic growth factors (HGFs) of  
1323 accumulation mode particles and their linkage to chemical composition in a heavily polluted urban atmosphere of  
1324 Kanpur at the Centre of IGP, India: Impact of ambient relative humidity, *Sci. Total Environ.*, 704, 135363,  
1325 doi:10.1016/j.scitotenv.2019.135363, 2020a.

1326 Mandariya, A. K., Tripathi, S. N., Gupta, T. and Mishra, G.: Wintertime hygroscopic growth factors (HGFs) of  
1327 accumulation mode particles and their linkage to chemical composition in a heavily polluted urban atmosphere of  
1328 Kanpur at the Centre of IGP, India: Impact of ambient relative humidity, *Sci. Total Environ.*, 704,  
1329 doi:10.1016/j.scitotenv.2019.135363, 2020b.

1330 Massling, A., Leinert, S., Wiedensohler, A. and Covert, D.: Hygroscopic growth of sub-micrometer and one-  
1331 micrometer aerosol particles measured during ACE-Asia, *Atmos. Chem. Phys.*, 7, 3249–3259 [online] Available  
1332 from: [www.atmos-chem-phys.net/7/3249/2007/](http://www.atmos-chem-phys.net/7/3249/2007/) (Accessed 30 October 2022), 2007.

1333 Maßling, A., Wiedensohler, A., Busch, B., Neusüß, C., Neusüß, N., Quinn, P., Bates, T. and Covert, D.:  
1334 Atmospheric Chemistry and Physics Hygroscopic properties of different aerosol types over the Atlantic and Indian  
1335 Oceans, *Atmos. Chem. Phys.*, 3, 1377–1397 [online] Available from: [www.atmos-chem-phys.org/acp/3/1377/](http://www.atmos-chem-phys.org/acp/3/1377/)  
1336 (Accessed 30 October 2022), 2003.

1337 Massoli, P., Lambe, A. T., Ahern, A. T., Williams, L. R., Ehn, M., Mikkilä, J., Canagaratna, M. R., Brune, W. H.,  
1338 Onasch, T. B., Jayne, J. T., Petäjä, T., Kulmala, M., Laaksonen, A., Kolb, C. E., Davidovits, P. and Worsnop, D.

1339 R.: Relationship between aerosol oxidation level and hygroscopic properties of laboratory generated secondary  
 1340 organic aerosol (SOA) particles, *Geophys. Res. Lett.*, 37(24), 1–5, doi:10.1029/2010GL045258, 2010.

1341 McFiggans, G., Artaxo, P., Baltensperger, U., Coe, H., Facchini, M. C., Feingold, G., Fuzzi, S., Gysel, M.,  
 1342 Laaksonen, A., Lohmann, U., Mentel, T. F., Murphy, D. M., O'Dowd, C. D., Snider, J. R. and Weingartner, E.:  
 1343 The effect of physical and chemical aerosol properties on warm cloud droplet activation, *Atmos. Chem. Phys.*,  
 1344 6(9), 2593–2649, doi:10.5194/acp-6-2593-2006, 2006.

1345 McNeill, V. F.: Aqueous organic chemistry in the atmosphere: Sources and chemical processing of organic  
 1346 aerosols, *Environ. Sci. Technol.*, 49(3), 1237–1244, doi:10.1021/es5043707, 2015.

1347 Mei, F., Setyan, A., Zhang, Q. and Wang, J.: CCN activity of organic aerosols observed downwind of urban  
 1348 emissions during CARES, *Atmos. Chem. Phys.*, 13(24), 12155–12169, doi:10.5194/acp-13-12155-2013, 2013.

1349 Ng, N. L., Herndon, S. C., Trimborn, A., Canagaratna, M. R., Croteau, P. L., Onasch, T. B., Sueper, D., Worsnop,  
 1350 D. R., Zhang, Q., Sun, Y. L. and Jayne, J. T.: An Aerosol Chemical Speciation Monitor (ACSM) for routine  
 1351 monitoring of the composition and mass concentrations of ambient aerosol, *Aerosol Sci. Technol.*, 45(7), 780–  
 1352 794, doi:10.1080/02786826.2011.560211, 2011.

1353 Ogawa, S., Setoguchi, Y., Kawana, K., Nakayama, T., Ikeda, Y., Sawada, Y., Matsumi, Y. and Mochida, M.:  
 1354 Hygroscopicity of aerosol particles and CCN activity of nearly hydrophobic particles in the urban atmosphere  
 1355 over Japan during summer, *J. Geophys. Res.*, 121(12), 7215–7234, doi:10.1002/2015JD024636, 2016.

1356 Petit, J. E., Favez, O., Albinet, A. and Canonaco, F.: A user-friendly tool for comprehensive evaluation of the  
 1357 geographical origins of atmospheric pollution: Wind and trajectory analyses, *Environ. Model. Softw.*, 88, 183–  
 1358 187, doi:10.1016/j.envsoft.2016.11.022, 2017.

1359 Petters, M. D. and Kreidenweis, S. M.: A single parameter representation of hygroscopic growth and cloud  
 1360 condensation nucleus activity, *Atmos. Chem. Phys. Atmos. Chem. Phys.*, 7, 1961–1971, doi:10.5194/acp-7-1961-  
 1361 2007, 2007.

1362 Prakash, J., Lohia, T., Mandariya, A. K., Habib, G., Gupta, T. and Gupta, S. K.: Chemical characterization and  
 1363 quantitativ e assessment of source-specific health risk of trace metals in PM1.0 at a road site of Delhi, India,  
 1364 *Environ. Sci. Pollut. Res.*, 25(9), 8747–8764, doi:10.1007/s11356-017-1174-9, 2018.

1365 Pringle, K. J., Tost, H., Pozzer, A., Pöschl, U. and Lelieveld, J.: Global distribution of the effective aerosol  
 1366 hygroscopicity parameter for CCN activation, *Atmos. Chem. Phys.*, 10(12), 5241–5255, doi:10.5194/acp-10-  
 1367 5241-2010, 2010.

1368 Rai, P., Furger, M., El Haddad, I., Kumar, V., Wang, L., Singh, A., Dixit, K., Bhattu, D., Petit, J.-E., Ganguly, D.,  
 1369 Rastogi, N., Baltensperger, U., Tripathi, S. N., Slowik, J. G. and Prévôt, A. S. H.: Real-time measurement and  
 1370 source apportionment of elements in Delhi's atmosphere, *Sci. Total Environ.*, 742, 140332, 2020,  
 1371 doi:10.1016/j.scitotenv.2020.140332, 2020.

1372 Randall, D A; Wood, R A; Bony, S; Colman, R; Fichefet, T; Fyfe, J; Kattsov, V; Pitman, A; Shukla, J; Srinivasan,  
 1373 J; Stouffer, R J; Sumi, A; Taylor, K. E.: Climate Models and Their Application, *Clim. Chang.* 2007 *Phys. Sci.*  
 1374 *Basis. Contrib. Work. Gr. I to Fourth Assess. Rep. Intergov. Panel Clim. Chang. Ed. by S. Solomon al.*, Cambridge  
 1375 Univ. Press. Cambridge, U. K., New York., Chapter 8(United Kingdom: N. p., p.2007. Web.), 590–662,  
 1376 doi:<http://www.ipcc.ch/pdf/assessment-report/ar4/wg1/ar4-wg1-chapter8.pdf>, 2007.

1377 Richard, A., Gianini, M. F. D., Mohr, C., Furger, M., Bukowiecki, N. and Minguill, M. C.: and Physics Source  
 1378 apportionment of size and time resolved trace elements and organic aerosols from an urban courtyard site in  
 1379 Switzerland, , 8945–8963, doi:10.5194/acp-11-8945-2011, 2011.

1380 Seinfeld, J. H. and Pandis, S. N.: Atmospheric cemistry and physics: From air pollution to climate change, Second  
 1381 edi., John Wiley & Sons, Inc., 2006.

1382 Shukla, A. K., Lalchandani, V., Bhattu, D., Dave, J. S., Rai, P., Thamban, N. M., Mishra, S., Gaddamidi, S.,  
 1383 Tripathi, N., Vats, P., Rastogi, N., Sahu, L., Ganguly, D., Kumar, M., Singh, V., Gargava, P. and Tripathi, S. N.:  
 1384 Real-time quantification and source apportionment of fine particulate matter including organics and elements in

1385 Delhi during summertime, *Atmos. Environ.*, 261, 118598, doi:10.1016/J.ATMOSENV.2021.118598, 2021.

1386 Sjogren, S., Gysel, M., Weingartner, E., Baltensperger, U., Cubison, M. J. and Coe, H.: Hygroscopic growth and  
1387 water uptake kinetics of two-phase aerosol particles consisting of ammonium sulfate, adipic and humic acid  
1388 mixtures, , 38, 157–171, doi:10.1016/j.jaerosci.2006.11.005, 2007.

1389 Sjogren, S., Gysel, M., Weingartner, E., Alfarra, M. R., Duplissy, J., Cozic, J., Crosier, J. and Coe, and U. B.:  
1390 Hygroscopicity of the submicrometer aerosol at the high-alpine site Jungfraujoch, 3580m a.s.l., Switzerland, ,  
1391 7231–7249, doi:10.5194/acp-12-7231-2012, 2012.

1392 Stokes, R. H. and Robinson, R. A.: Interactions in Aqueous Nonelectrolyte Solutions. I. Solute-Solvent Equilibria,  
1393 *J. Phys. Chem.*, 70(7), 2126–2131, doi:10.1021/j100879a010, 1966.

1394 Su, H., Rose, D., Cheng, Y. F., Gunthe, S. S., Massling, A., Stock, M., Wiedensohler, A., Andreae, M. O. and  
1395 Pöschl, U.: Hygroscopicity distribution concept for measurement data analysis and modeling of aerosol particle  
1396 mixing state with regard to hygroscopic growth and CCN activation, *Atmos. Chem. Phys.*, 10, 7489–7503,  
1397 doi:10.5194/acp-10-7489-2010, 2010.

1398 Sun, Y., Wang, Z., Fu, P., Jiang, Q., Yang, T., Li, J. and Ge, X.: The impact of relative humidity on aerosol  
1399 composition and evolution processes during wintertime in Beijing, China, *Atmos. Environ.*, 77, 927–934,  
1400 doi:10.1016/j.atmosenv.2013.06.019, 2013.

1401 Sun, Y., Du, W., Fu, P., Wang, Q., Li, J., Ge, X., Zhang, Q., Zhu, C., Ren, L., Xu, W., Zhao, J., Han, T., Worsnop,  
1402 D. R. and Wang, Z.: Primary and secondary aerosols in Beijing in winter: Sources, variations and processes,  
1403 *Atmos. Chem. Phys.*, 16(13), 8309–8329, doi:10.5194/acp-16-8309-2016, 2016.

1404 Swietlicki, E., Hansson, H. C., Hämeri, K., Svenningsson, B., Massling, A., McFiggans, G., McMurry, P. H.,  
1405 Petäjä, T., Tunved, P., Gysel, M., Topping, D., Weingartner, E., Baltensperger, U., Rissler, J., Wiedensohler, A.  
1406 and Kulmala, M.: Hygroscopic properties of submicrometer atmospheric aerosol particles measured with H-  
1407 TDMA instruments in various environments—a review, *Tellus B Chem. Phys. Meteorol.*, 60(3), 432–469,  
1408 doi:10.1111/j.1600-0889.2008.00350.x, 2008.

1409 Tang, I. N. and Munkelwitz, H. R.: Water activities, densities, and refractive indices of aqueous sulfates and  
1410 sodium nitrate droplets of atmospheric importance, *J. Geophys. Res.*, 99(D9), 18801, doi:10.1029/94JD01345,  
1411 1994.

1412 Tobler, A., Bhattu, D., Canonaco, F., Lalchandani, V., Shukla, A., Thamban, N. M., Mishra, S., Srivastava, A. K.,  
1413 Bisht, D. S., Tiwari, S., Singh, S., Močnik, G., Baltensperger, U., Tripathi, S. N., Slowik, J. G. and Prévôt, A. S.  
1414 H.: Chemical characterization of PM2.5 and source apportionment of organic aerosol in New Delhi, India, *Sci.  
1415 Total Environ.*, 745, 140924, doi:10.1016/J.SCITOTENV.2020.140924, 2020.

1416 Topping, D. O. and McFiggans, G.: Tight coupling of particle size, number and composition in atmospheric cloud  
1417 droplet activation, *Atmos. Chem. Phys.*, 12(7), 3253–3260, doi:10.5194/acp-12-3253-2012, 2012.

1418 Tritscher, T., Jumyi, Z., Martin, M., Chirico, R., Gysel, M., Heringa, M. F., Decarlo, P. F., Sierau, B., Prévôt, A.  
1419 S. H., Weingartner, E. and Baltensperger, U.: Changes of hygroscopicity and morphology during ageing of diesel  
1420 soot, *Environ. Res. Lett.*, 6(3), doi:10.1088/1748-9326/6/3/034026, 2011.

1421 Wang, X., Shen, X. J., Sun, J. Y., Zhang, X. Y., Wang, Y. Q., Zhang, Y. M., Wang, P., Xia, C., Qi, X. F. and  
1422 Zhong, J. T.: Size-resolved hygroscopic behavior of atmospheric aerosols during heavy aerosol pollution episodes  
1423 in Beijing in December 2016, , 194(September), 188–197, doi:10.1016/j.atmosenv.2018.09.041, 2018a.

1424 Wang, Y., Wu, Z., Ma, N., Wu, Y., Zeng, L., Zhao, C. and Wiedensohler, A.: Statistical analysis and  
1425 parameterization of the hygroscopic growth of the sub-micrometer urban background aerosol in Beijing, *Atmos.  
1426 Environ.*, 175(December 2017), 184–191, doi:10.1016/j.atmosenv.2017.12.003, 2018b.

1427 Wester, P., Mishra, A., Mukherji, A., Shrestha, A. B. and Change, C.: The Hindu Kush Himalaya Assessment,  
1428 edited by P. Wester, A. Mishra, A. Mukherji, and A. B. Shrestha, Springer International Publishing, Cham., 2019.

1429 Wu, Z. J., Poulain, L., Henning, S., Dieckmann, K., Birmili, W., Merkel, M., van Pinxteren, D., Spindler, G.,

1430 Müller, K., Stratmann, F., Herrmann, H. and Wiedensohler, A.: Relating particle hygroscopicity and CCN activity  
1431 to chemical composition during the HCCT-2010 field campaign, *Atmos. Chem. Phys.*, 13(16), 7983–7996,  
1432 doi:10.5194/acp-13-7983-2013, 2013a.

1433 Wu, Z. J., Poulain, L., Henning, S., Dieckmann, K., Birmili, W., Merkel, M., Van Pinxteren, D., Spindler, G.,  
1434 Stratmann, F., Herrmann, H. and Wiedensohler, A.: Sciences ess Atmospheric Chemistry and Physics Climate of  
1435 the Past Geoscientific Instrumentation Methods and Data Systems Relating particle hygroscopicity and CCN  
1436 activity to chemical composition during the HCCT-2010 field campaign, *Atmos. Chem. Phys.*, 13, 7983–7996,  
1437 doi:10.5194/acp-13-7983-2013, 2013b.

1438 Wu, Z. J., Zheng, J., Shang, D. J., Du, Z. F., Wu, Y. S., Zeng, L. M., Wiedensohler, A. and Hu, M.: Particle  
1439 hygroscopicity and its link to chemical composition in the urban atmosphere of Beijing , China , during  
1440 summertime, , 1123–1138, doi:10.5194/acp-16-1123-2016, 2016.

1441 Yeung, M. C., Lee, B. P., Li, Y. J. and Chan, C. K.: Simultaneous HTDMA and HR -ToF-AMS measurements at  
1442 the HKUST supersite in Hong Kong in 2011, *J. Geophys. Res.*, 119(16), 9864–9883, doi:10.1002/2013JD021146,  
1443 2014.

1444 Zhang, Q., Jimenez, J. L., Worsnop, D. R. and Canagaratna, M.: A Case Study of Urban Particle Acidity and Its  
1445 Influence on Secondary Organic Aerosol, *Environ. Sci. Technol.*, 41(9), 3213–3219, doi:10.1021/es061812j,  
1446 2007.

1447 Zhang, S. L., Ma, N., Kecorius, S., Wang, P. C., Hu, M., Wang, Z. B., Größ, J., Wu, Z. J. and Wiedensohler, A.:  
1448 Mixing state of atmospheric particles over the North China Plain, *Atmos. Environ.*, 125, 152–164,  
1449 doi:10.1016/j.ATMOSENV.2015.10.053, 2016.

1450 Zhang, Y., Tang, L., Yu, H., Wang, Z., Sun, Y., Qin, W., Chen, W., Chen, C., Ding, A., Wu, J., Ge, S. and Chen,  
1451 C.: Chemical composition , sources and evolution processes of aerosol at an urban site in Yangtze River Delta ,  
1452 China during wintertime, *Atmos. Environ.*, 123, 339–349, doi:10.1016/j.atmosenv.2015.08.017, 2015.

1453 Zhao, P., Du, X., Su, J., Ding, J. and Dong, Q.: Aerosol hygroscopicity based on size-resolved chemical  
1454 compositions in Beijing, *Sci. Total Environ.*, 716, 137074, doi:10.1016/j.SCITOTENV.2020.137074, 2020.

1455